Annales Geophysicae

Generation of mesoscale F layer structure and electric fields by the combined Perkins and E_s layer instabilities, in simulations

R. B. Cosgrove

Center for Geospace Studies, SRI International, Menlo Park, CA, USA

Abstract. The generic equilibrium configuration of the nighttime midlatitude ionosphere consists of an F layer held up against gravity by winds and/or electric fields, and a sporadic E (E_s) layer located by a sheared wind field, which experiences the same electric fields as the F layer. This configuration is subject to two large-scale (e.g. >10 km) "layer instabilities": one of the F layer known as the Perkins instability, and another of the E_s layer which has been called the E_s layer instability. Electric fields on scales larger than (about) 10 km map very efficiently between the E_s and F layers, and the two instabilities have a similar geometry, allowing them to interact with one another. As shown through a linear growth rate analysis, the two most important parameters governing the interaction are the relative horizontal velocity between the E_s and F layers, and the integrated conductivity ratio Σ_H / Σ_{PF}, where Σ_H and Σ_{PF} are the field line integrated Hall conductivity of the E_s layer, and the field line integrated Pedersen conductivity of the F layer, respectively. For both large and small relative velocities the growth rate was found to be more than double that of the Perkins instability alone, when $\frac{\Sigma_H}{\Sigma_{PF}}{=}1.8$. However, the characteristic eigenmode varies considerably with relative velocity, and different nonlinear behavior is expected in these two cases. As a follow up to the linear growth rate analysis, we explore in this article the nonlinear evolution of the unstable coupled system subject to a 200 km wavelength initial perturbation of the F layer, using a two-dimensional numerical solution of the two-fluid equations, as a function of relative horizontal velocity and $\frac{\Sigma_H}{\Sigma_{PF}}$. We find that when $\frac{\Sigma_H}{\Sigma_{PF}} \overset{\sim}{<} 0.5$ the Perkins instability is able to control the dynamics and modulate the F layer altitude in 2 to 3 h time. However, the electric fields remain small until the altitude modulation is extremely large, and even then they are not large enough to account for the observations of large midlatitude electric

fields. When $\frac{\Sigma_H}{\Sigma_{PF}} \overset{\sim}{>} 1$ the E_s layer becomes a major contributor to the F layer dynamics. The E_s layer response involves the breaking of a wave, with associated polarization electric fields, which modulate the F layer. Larger electric fields form when the relative velocity between the E_s and F layers is large, whereas larger modulations of the F layer altitude occur when the relative velocity is small. In the latter case the F layer modulation grows almost twice as fast (for $\frac{\Sigma_H}{\Sigma_{PF}}{=}1$) as when no E_s layer is present. In the former case the electric fields associated with the E_s layer are large enough to explain the observations (~ 10 mV/m), but occur over relatively short temporal and spatial scales. In the former case also there is evidence that the F layer structure may present with a southwestward trace velocity induced by E_s layer motion.

Keywords. Ionosphere (Ionospheric irregularities; Midlatitude ionosphere; Plasma waves and instabilities)

1 Introduction

1.1 Model and relevant observations

The generic equilibrium configuration of the nighttime midlatitude ionosphere consists of an F layer held up against gravity by winds and/or electric fields, and a sporadic E (E_s) layer located by a sheared wind field, which experiences the same electric fields as the F layer. This configuration is subject to two large-scale (e.g., >10 km) "layer instabilities": one of the F layer known as the Perkins instability (Perkins, 1973), and another of the E_s layer which has been called the E_s layer instability (Cosgrove and Tsunoda, 2002b). By a "layer instability" we mean an instability of field line integrated (FLI) quantities, where the field line integration is across a plasma layer. Examples of FLI quantities include the total electron content (TEC), and the layer altitude (obtained

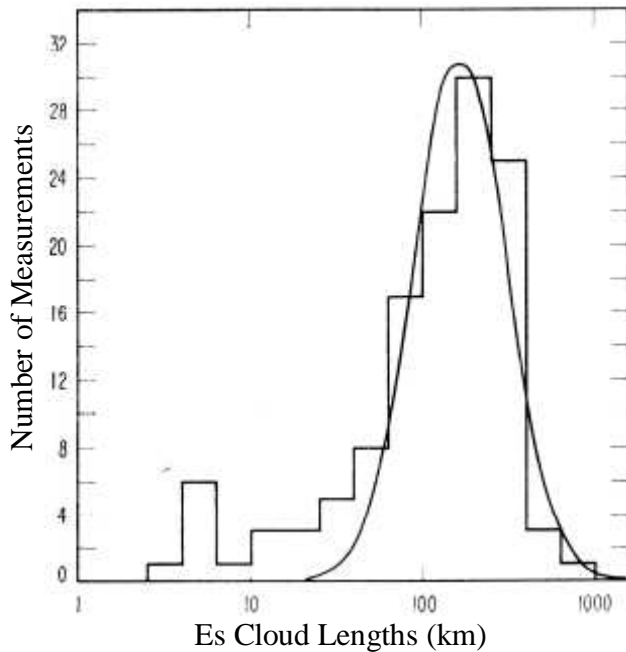*Correspondence to:* R. B. Cosgrove
(russell.cosgrove@sri.com)

Fig. 1. Histogram of E_s lengths, at 7.22 MHz, with a log normal fit to the longer dimensions. The fit has its peak at 170 km, and approximately 68% of the area under the curve lies in the interval 94 km to 310 km. Reproduced from Cathey (1969).

by integrating the product of altitude and density, and dividing the result by TEC). Because electric fields on scales larger than about 10 km map very efficiently between the E_s and F layers (Farley, 1960; Spreiter and Briggs, 1961), the system consists of two interacting unstable layers, which form a coupled E_s-F layer system. Therefore, the interaction of these two unstable layers should govern the system electrodynamics on scales from 10 km up to the upper limit wavelength of the horizontal spatial spectrum of the E_s distribution. In this paper we study the nonlinear coupled electrodynamics of the E_s layer and F layer (Perkins) instabilities, on the spatial scale of F region structuring events observed in all sky images, using a numerical solution of the two-fluid equations.

A peculiar feature of both the Perkins and E_s layer instabilities is the fact that the growth rates maximize for waves with phase fronts aligned from northwest to southeast (southwest to northeast) in the Northern (Southern) Hemisphere. It is therefore noteworthy that observations in the nighttime midlatitude ionosphere tend to find frontal structures with this same alignment, whenever the horizontal viewing area is sufficiently large. Spaced ionosonde observations (Goodwin and Summers, 1970), and coherent scatter radar observations (Yamamoto et al., 1994, 1997; Hysell et al., 2004) show nighttime E_s layer structure in the Northern (Southern) Hemisphere with a clear statistical tendency to form fronts

elongated from northwest to southeast (southwest to northeast), and generally propagating to the southwest (northwest). Similarly for the F layer, all sky images (e.g., Garcia et al., 2000; Kubota et al., 2001; Saito et al., 2001; Shiokawa et al., 2003) show nighttime structure with the same clear statistical tendency to form fronts, with the same alignment and propagation direction. We will refer to the F region observations as mesoscale traveling ionospheric disturbances (MSTIDs).

Although rare, midlatitude events involving large polarization electric fields have also been observed, and these display the same frontal alignment. Behnke (1979), using the Arecibo incoherent scatter radar (ISR), observed a Doppler velocity in the F layer exceeding 400 m/s, suggesting an electric field greater than 17 mV/m, which was associated with a sharp 80 km rise in the F layer altitude. The disturbance was in the form of a band propagating to the southwest at about 50 m/s, which matches the maximum growth rate orientation noted above. Behnke (1979) presents five similar disturbances, and notes a wavelength of 230 km for the most wavelike example. Another observation of large F region Doppler velocities, exceeding 250 m/s, was made by Fukao et al. (1991), who used the 50 MHz MU radar in Japan to observe coherent backscatter. However, the experimental geometry did not permit observation of a horizontally extended region. Because simultaneous all sky images are not available for any of these large polarization field events, the extent to which they are related to the nighttime MSTID events described above remains unclear.

Because of the peculiar orientation associated with the phenomena just described, the Perkins instability was in both cases identified as the most likely source. However, our results below indicate that E_s layers may also be an important contributor to the electrodynamics of the nighttime midlatitude ionosphere, and that therefore both phenomena should be studied in terms of an E_s-F two-layer system coupled by electric field mapping. The wavelength for MSTIDs ranges from 50 km to 300 km, with a preference for about 200 km (Garcia et al., 2000; Shiokawa et al., 2003). The wavelength of 230 km noted by Behnke (1979) for the large electric field events falls in the same range. Cathey (1969) published a histogram of E_s layer horizontal scale sizes derived from a satellite born ionospheric sounder, which we reproduce here as Fig. 1. Figure 1 shows a central peak at 170 km, which covers almost exactly the wavelength range observed for MSTIDs. The sounder operated at a frequency of 7.22 MHz, and layers were considered distinct if there was no backscatter over 20 miles. Although shorter scale structures are often observed, this study appears to show that the horizontal spatial spectrum of E_s distributions covers the mesoscale range. The idea that E_s layers can support mesoscale electrodynamics is also supported by spaced ionosonde experiments. For example, Goodwin (1966) reported correlated E_s layer structures over as much as 1000 km.

It has been often noted that the Perkins instability has a rather small growth rate, and that the modes of the Perkins instability should generally propagate to the northeast, not to the southwest (Garcia et al., 2000). Whether or not E_s layer effects may nullify these concerns is one of the issues to be discussed below. We find that when an E_s layer is present with $\frac{\Sigma_H}{\Sigma_{PF}} \overset{\sim}{>} 1$, then larger polarization electric fields are generated in a shorter period of time, where Σ_H and Σ_{PF} are the FLI Hall conductivity of the E_s layer, and the FLI Pedersen conductivity of the F layer, respectively. In addition, there is evidence in the simulations that E_s induced structuring of the F layer may present with a southwestward trace velocity induced by E_s layer motion. However, we also find that when E_s layer effects are negligible the Perkins instability is able to control the dynamics and modulate the F layer altitude in 2 to 3 h time, although large polarization fields do not arise until the F layer altitude has been modulated in excess of 100 km. Finally, we note that E_s layer structuring coincident with midlatitude F region structuring has been described by a number of authors (see Sect. 1.2), and our simulations certainly show a similar effect caused by the E_s layer instability.

In this study, we are considering the creation of structure by an instability, and therefore we initiate the simulations in the equilibrium configuration which is unstable, except for a small seed perturbation. The unstable equilibrium is uniform E_s and F layers, and hence the simulation is initiated in this way, except for a 200 km wavelength ±5 km modulation of the F layer altitude, which serves as the seed. The wavelength is chosen to address the F layer observations noted above. One shorter wavelength initialization is also presented. Gravity waves could create the initial F layer modulation. We choose an initial F layer modulation instead of an E_s layer modulation because 200 km wavelength gravity waves are expected to be negligible at E_s layer altitudes, but can be significant in the F layer.

As the name "sporadic" implies, E_s layers generally display structure on scales much shorter than 200 km. The effects of preexisting shorter scale structure on the mesoscale electrodynamics, sometimes referred to as anomalous effects, will not be considered in this study. Some of the shorter scale structure that has been observed can possibly be explained by the same theory. Previous simulations (Cosgrove and Tsunoda, 2003) have investigated 30 km wavelength waves in E_s layers, in connection with the QP echo phenomena (but not their effect on the F layer). Therefore, another approach might be to seed the simulation with a broadband perturbation, if a realistic one could be determined. However, there may be additional sources of short scale structure that cannot be modeled in the present framework, such as neutral turbulence. In these initial studies (the present one and Cosgrove and Tsunoda, 2003) we have chosen the seed perturbations so as to probe localized regions of wavenumber space. We consider the effects of smaller scale structure on the development of the mesoscale structure to be

a separate topic, to be dealt with in a subsequent study.

There is also the possibility of nonlinear electrodynamical effects coupling energy to shorter wavelengths. Because the simulations presented here assume unattenuated mapping of $\boldsymbol{E}$ along $\boldsymbol{B}$, they do not capture some other phenomena that could be involved in nonlinear coupling to shorter wavelengths. Shorter scale wavelengths do not map as efficiently to the F region, so the assumption in this simulation that the electric field maps unattenuated to the F region acts to suppress possible nonlinear development of shorter scale structure in the E_s layer. Also, the nonlocal gradient drift instability (Rosado-Roman et al., 2004; Seyler et al., 2004) and the collisional drift instability (Hysell et al., 2002) operate through incomplete electric field mapping and/or parallel to $\boldsymbol{B}$ currents, and hence are not captured in this simulation. For a summary of the observational support for the E_s layer instability see Tsunoda et al. (2004).

1.2 History and place

The idea that the nighttime midlatitude ionosphere should be regarded as an E_s-F coupled electrodynamical system goes back to Bowman (1960), who presented evidence that frontal structures in the F layer were associated with similar frontal structures in the E_s layer. Goodwin (1966) presented additional observations supporting Bowman's findings. Tsunoda and Cosgrove (2001) found that there was a positive reinforcement between altitude modulations of the E_s and F layers, and pointed out that the apparent presence of a Hall-current-driven polarization process in E_s layers (Haldoupis et al., 1996; Tsunoda, 1998; Cosgrove and Tsunoda, 2001, 2002a) gave new importance to the idea of E_s-F coupling. After discovery of the E_s layer instability Cosgrove and Tsunoda (2004a) revisited the E_s-F coupling problem, and provided a unified formalism for the Perkins and E_s layer instabilities, which is the linear theory for the system studied through simulations in the present paper.

During the same period Mathews et al. (2001a), and Swartz et al. (2002), presented high resolution ISR measurements showing apparent electrodynamic linkage between the F and E_s layers. In companion papers, Kelley et al. (2003) and Haldoupis et al. (2003) have also argued for interpreting the E_s and F layers as a coupled system, although they do not invoke the E_s layer instability of Cosgrove and Tsunoda (2002b). The model presented by Haldoupis et al. (2003) for E_s-F coupling was later supported by a computation of the magnitude of the associated polarization electric field by Shalimov and Haldoupis (2005), who found that the large (on the order of 100 m/s) neutral winds that have been found in the vicinity of E_s layers (Larsen et al., 1998; Larsen, 2002) can create electric fields on the order of 10 mV/m, depending on the specific conditions. Their calculation is based on the assumption of the pre-existence of isolated elongated E_s patches (strips), together with the F region current closure model for E_s polarization given by Shalimov et al. (1998).

This F region current closure model involves closure of the electrojet-like current, associated with a polarization field transverse to the E_s strip, through the F layer. This mechanism becomes particularly important when the transverse scale is short enough that the polarization electric fields do not map efficiently to the F layer. In addition to the original analytical formulation by Shalimov et al. (1998), simulations by Hysell and Burcham (2000), and by Hysell et al. (2002) have verified the F region closure model, and even led to the discovery of a collisional drift instability that may be important for generating 1 km scale structures in E_s layers. Hence, the Haldoupis et al. (2003) E_s-F coupling model allows for explanation of F region structures, with scales matching the scales of isolated E_s patches generated by some other source, without invoking wind shear.

The model advanced by Cosgrove and Tsunoda (2004a), which is simulated herein, differs from the Haldoupis et al. (2003) model in that it is a dynamical model that attempts to explain F region structure starting from flat, horizontally stratified E_s and F layers, by invoking the E_s layer instability together with the Perkins instability. It is a two-dimensional model, based on the two-dimensional nature of the simplest E_s layer and Perkins instability formulations. As such it does not fully include the Shalimov and Haldoupis (2005) formulation, which is three-dimensional, due to their desire to treat E_s patches that are not highly elongated. In the present work a two-dimensional simulation is justified because the modes of the instabilities are naturally plane waves.

Yokoyama et al. (2004) simulated the E_s layer instability in three dimensions, using a finite length for the phase fronts of the plane-wave-like modes. They found growth of the instability consistent with the two-dimensional model, but were not able to make a significant study of nonlinearities, and the possible growth of three dimensional E_s structures, due to grid size constraints. They did, however, study another important difference between the Shalimov et al. (1998) model, and the Cosgrove and Tsunoda (2004a) model, which is that the inclusion of E region wind shear in the latter means that closure of the electrojet-like E_s layer currents can occur substantially within the E_s layer itself. This effect allows large electric fields to be generated by continuous E_s layers, without highly elongated structures, and without forming isolated E_s patches (Cosgrove and Tsunoda, 2001, 2002a). In the simulations presented below both current closure paths are available, however, the structures are always highly elongated (i.e. two-dimensional), and always assume transverse scales larger than 10 km (so that E fields map along B), so that some important three dimensional and short scale effects discovered by Shalimov et al. (1998), and Shalimov and Haldoupis (2005), cannot be studied.

2   Physics of the E_s-F system

The Perkins instability is an instability of the F layer to an altitude modulation horizontally distributed as a plane wave. The azimuthal orientation of the plane wave phase fronts that maximizes the growth rate depends on the effective background electric field direction, but is typically northwest to southeast (northeast to southwest) in the Northern (Southern) Hemisphere, due to a northward (southward) effective electric field component. The vertical gradient in neutral density coupled with a meridional component of the electric field (or equivalent neutral wind) contributes the free energy for the instability through a Pedersen-current-driven polarization process; because of the gradient in neutral density, the FLI conductivity of the layer changes when its' altitude changes. However, the growth rate is generally quite small, for example $0.0001\,\mathrm{s}^{-1}$.

The $E_s\mathrm{L}$ instability is an instability of the E_s layer to an altitude modulation horizontally distributed as a plane wave, with coupling to similarly distributed FLI density modulations. (The compressibility of E region plasma allows FLI density modulations.) The azimuthal orientation of the plane wave phase fronts that maximizes the growth rate is northwest to southeast (northeast to southwest) in the Northern (Southern) Hemisphere. The shear in the zonal component of the neutral wind that forms the layer, possibly aided by a meridional wind, contributes the free energy for the instability through a Hall-current-driven polarization process. The variation of neutral density with altitude is in this case negligible compared to the variation in wind velocity with altitude. However, significant FLI conductivity modulations are caused by FLI density modulations. Because the wind shear can be quite large (Larsen et al., 1998; Larsen, 2002), and because the Hall to Pedersen conductivity ratio enters the polarization process, the growth rate (in the absence of an F layer) is generally much larger than that for the Perkins instability, for example $0.005\,\mathrm{s}^{-1}$.

For wavelengths long enough for the polarization fields to map between the E_s and F layers, the layers are resistive loads for one another. At first glance (i.e. ignoring any dynamical interaction) one might expect that this would reduce the growth rates in both layers (Klevens and Imel, 1978). The FLI Pedersen conductivity of the F layer is generally much larger than that of the E_s layer. Hence, the F layer should (by this simple reasoning) reduce the growth rate of the $E_s\mathrm{L}$ instability much more than the $E_s\mathrm{L}$ reduces the growth rate of the Perkins instability. Nevertheless, the FLI Hall conductivity of a dense E_s layer can often exceed the FLI Pedersen conductivity of the F layer, and the growth rate expression suggests that in this case the E_s layer instability can still be quite active. Cosgrove and Tsunoda (2003) have confirmed this using simulations.

These considerations are conclusive to the extent that the effect of the F layer on the E_s layer instability (and vice versa) is one of a static load. But in fact the F layer is

unstable to the Perkins instability, and the modes of the Perkins instability have the right geometry for coupling to the modes of the E_sL instability, via the mapping of polarization electric fields along magnetic field lines. In Cosgrove and Tsunoda (2004b) the dynamical interaction of the two instabilities was described using schematic diagrams, and an approximate analytical expression for the growth rate was derived. It was shown that, subject to a resonance condition, the coupled system growth rate is substantially larger than that of either the E_s layer or Perkins instabilities, loaded by static F or E_s layers, respectively. Because a static E_s layer would have little effect on the much more highly conducting F layer, this implies that the growth rate for F region structure can be enhanced when an E_s layer is present in a wind shear environment.

The Cosgrove and Tsunoda (2004b) analysis just referred to is valid when the E_s and F layers have the same horizontal velocity, which they show occurs when the eastward component of the effective electric field at the E_s layer altitude is zero. We refer to this as spatial resonance in the present paper. Specifically, spatial resonance occurs when $E' \cdot \hat{e} = (E + u_{E_s} \times B) \cdot \hat{e} = 0$, where $\hat{e}$ is an eastward directed unit vector and u_{E_s} is the wind in the E_s layer. The parameter $E' \cdot \hat{e}$ parameterizes the "amount" of dynamical coupling between the two instabilities, for a variety of background electric field, and E_s layer wind conditions. When $E' \cdot \hat{e} \neq 0$ the waves associated with the Perkins and E_s layer instabilities have a nonzero relative phase velocity. If the wavelength divided by the relative phase velocity (the time to move a wavelength) is less than or on the order of the e-folding time for the coupled instability, then the E_s and F layers do not have a significant dynamical interaction in the linear theory. On the other hand, when $E' \cdot \hat{e} \neq 0$ there is a zeroth order current in the E_s layer, and this causes FLI density modulations of the E_s layer to couple to altitude modulations of the E_s layer (Cosgrove and Tsunoda, 2002b), which increases the growth rate of the E_s layer instability (as computed with a stable (static) F layer).

Cosgrove and Tsuonda (2004a) derived the linear growth rate of the E_s-F layer coupled system as a function of $E' \cdot \hat{e}$, F layer wind, and E_s layer wind shear. When $E' \cdot \hat{e} = 0$ there is only one instability (one unstable mode), which indicates a dynamical interaction of the E_s layer and Perkins instabilities. When $E' \cdot \hat{e}$ is greatly different from zero, the theory gives two independent unstable modes, with growth rates corresponding to the individual E_s layer and Perkins instabilities, loaded by static F and E_s layers, respectively. In general, there is a partial dynamical coupling of the two instabilities, and two unstable modes, with growth rates different from the simple E_s layer and/or Perkins instabilities. In all cases the electric fields generated by the instabilities are present in both the E_s and F layers, and cause structuring in both layers.

Therefore, in order to understand the distinct manifestations of the unstable dynamics of the coupled system, we will perform numerical simulations under the two extreme cases of zero relative velocity ($E' \cdot \hat{e} = 0$, the resonant case), and large relative velocity ($E' \cdot \hat{e} \gg 0$, the non-resonant case). Note that the intent is to provide an understanding of the system characteristics, and not to model a particular days events.

3 Simulation method

In this paper we perform two-dimensional numerical solutions of the two-fluid equations governing an F layer with winds and electric fields, and an E_s layer with sheared winds and electric fields, coupled by the assumption that the electric field maps unattenuated between, and through (except for an ambipolar electric field), the F and E_s layers. Since we only consider scales on the order of 10 km and greater the latter assumption is a good one (Farley, 1960; Spreiter and Briggs, 1961). Since a growing mode of the instability is a plane wave, the direction along the phase front of the wave is an invariant direction. Hence, the time evolution problem for these modes is two-dimensional. Of course, only plane-wave-like distortions with finite length phase fronts can be physical. An analytical solution for the polarization field in an analogous finite length structure has been obtained by Cosgrove and Tsunoda (2001). It shows that the structure must be elongated to support the polarization field. Hence, we expect realistic unstable modes to have a reduced-dimensional character. This justifies the use of a two-dimensional simulation as a tool for studying the nonlinear evolution of the unstable layers. The linear theory shows that the growth rate maximizes when the phase fronts of the growing plane wave modes are aligned northwest to southeast. Hence, we will perform a two-dimensional simulation with this orientation. Because of the skewed geometry with respect to B, there are some subtleties involved in correctly reducing the computation domain to two dimensions, which are explained in Sect. 3.1.

3.1 Layer geometry and simulation domain

The growing modes of the Perkins and E_s layer instabilities are plane wave altitude modulations. To describe the geometry of the modes and the reduction to a two-dimensional simulation we refer to the paper model of an altitude modulated E_s layer shown in Fig. 2, which, with the exception of the altitude notations and wind vectors, can equally well represent the F layer. Figure 2 shows two strips with horizontal long axes oriented southeast to northwest, which we call the $\hat{x}$ direction. The red strip is raised above the equilibrium altitude, and the blue strip is lowered below the equilibrium altitude. Although the figure cannot show it, the strips are very long in the $\hat{x}$ direction, which therefore is an invariant direction; all physical quantities are invariant under translations in the $\hat{x}$ direction. In particular, current can flow in the $\hat{x}$ direction without causing polarization charge to build up, which means
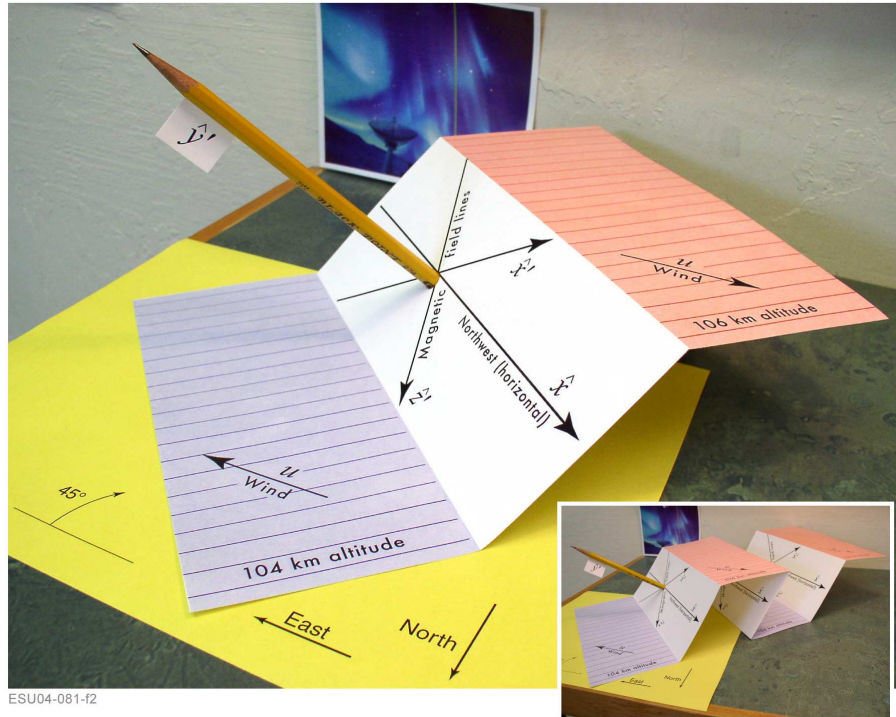
Fig. 2. Three-dimensional view of the E_s layer instability geometry.

that any polarization electric field must be perpendicular to $\hat{x}$. Since the polarization electric field must also be perpendicular to the magnetic field, which we take to be along $\hat{z}'$, it is constrained to be parallel (or anti-parallel) to the direction shown as $\hat{y}'$ in the figure. The primed coordinate system is completed by adding $\hat{x}'=\hat{y}'\times\hat{z}'$. It is apparent from Fig. 2 that the $\hat{x}$ and $\hat{x}'$ axes are connected by magnetic field lines, which means that the $\hat{x}'$ direction must be an invariant direction for FLI quantities, and for the electric field (which is assumed to map along $\boldsymbol{B}$).

The two-dimensional simulation plane will be the $\hat{y}'-\hat{z}'$ plane, which contains the polarization electric field and the magnetic field. As will be evident from the calculation described in Sect. 3.2, with the assumption that $\boldsymbol{E}$ maps along $\boldsymbol{B}$ the polarization electric field depends only on FLI quantities, and therefore varies in only one direction, the $\hat{y}'$ direction. As described above, it is also directed in the $\hat{y}'$ direction. Therefore, it is trivially curl free, and its' computation is a one-dimensional problem, which is achieved algebraically, without the need for an elliptical solver, as described in Sects. 3.2–3.3.

The three-dimensional ion velocity is computed from the polarization electric field and the neutral wind velocity, the latter of which we take to be the rotational wind field (see Sect. 4):

$$\boldsymbol{u} = u_N \cos(k_s z + \phi)\hat{n} + u_E \sin(k_s z + \phi)\hat{e}, \qquad (1)$$

where $\hat{n}$ is northward, $\hat{e}$ is eastward, and z is the altitude (positive downward). (The phase ϕ will be chosen so that $z=0$ is the exact equilibrium altitude of the E_s layer.) Note that the three-dimensional plasma velocity does not necessarily lie in the simulation plane, and this may seem, at first, to be a problem. However, because of the symmetry in the x-direction, the ion velocity component in the x-direction (v_{ix}) is "pure gauge," that is, it has no effect on the evolution of the ion density. All three velocity components ($v_{ix'}$, $v_{iy'}$, and $v_{iz'}$) depend on the gauge variable v_{ix}. Because v_{ix} has no effect on the ion density evolution, we can simply set it so that the three-dimensional velocity lies everywhere in the $\hat{y}'-\hat{z}'$ plane ($v_{ix'}=0$), and thereby formulate the plasma evolution as two-dimensional, in the plane containing the electric field and the magnetic field. This is expected. Whenever there is a symmetry it is possible to reduce the dimensionality of the problem (e.g. Stephani, 1995).

The model equations described in Sect. 3.2 will be solved on simulation grids covering the $\hat{y}'-\hat{z}'$ plane, one for the E_s layer and one for the F layer. A 201×100 grid with 2 km square cells is employed for the F region, and an $N\times2000$ grid with 100 m square cells is employed for the E_s layer, where N is either 70, 140, or 280, as required to contain the E_s layer. However, the grid edges are not placed along $\hat{y}'$ and $\hat{z}'$. By choosing to do the simulations at a magnetic field dip angle of 35° the magnetic and polarization fields are oriented in the simulation plane at 45°

about the horizontal direction, as shown in Fig. 3. The axes shown in Fig. 3 indicate the orientations of the grid edges, which are horizontal (roughly northeast), and upward with a tilt toward the southeast. (Specifically, the abscissa is directed along $0.87\hat{n}+0.50\hat{e}$, and the ordinate is directed along $-0.29\hat{n}+0.50\hat{e}-0.82\hat{z}$.) These are the axes used to display the simulation results. The electric field is expressed in terms of field line integrated quantities in Sect. 3.2. With this grid choice field line integration can be carried out by summing along the grid diagonals. The F region FLI quantities are interpolated at the boundary to match onto the E region grid, so that the field line integration extends across both the E_s and F layers.

3.2 Flux-conservative initial value problem

Sporadic E layers in the nighttime midlatitude E region are thought to be made up of long lived metallic ions, so that on the scale of a few hours E_s layer evolution is essentially an electrodynamic problem. Assuming a sufficiently high altitude, F region recombination is also a slow process, such that the F layer lasts throughout the night. Therefore, we will solve the two-fluid equations without the generation and recombination terms. Using the quasi-neutrality ($n_i=n_e=n$) and the isothermal ($T_i=T_e=T$) approximations, the steady state two-fluid equations for the motions of ions and electrons may be written

$$\frac{e}{M_i}(\boldsymbol{E} + \boldsymbol{v}_i \times \boldsymbol{B}) - \frac{T\nabla n}{M_i n} + \nu_i(\boldsymbol{u} - \boldsymbol{v}_i) + \boldsymbol{g} = 0 \qquad (2)$$

$$-\frac{e}{M_e}(\boldsymbol{E} + \boldsymbol{v}_e \times \boldsymbol{B}) - \frac{T\nabla n}{M_e n} + \nu_e(\boldsymbol{u} - \boldsymbol{v}_e) + \boldsymbol{g} = 0 \qquad (3)$$

$$\frac{\partial n}{\partial t} + \nabla \cdot (n\boldsymbol{v}_i) = 0 \qquad (4)$$

$$\frac{\partial n}{\partial t} + \nabla \cdot (n\boldsymbol{v}_e) = 0, \qquad (5)$$

where n is the plasma density, $\boldsymbol{v}_i$ is the velocity of the ions, $\boldsymbol{v}_e$ is the velocity of the electrons, $\boldsymbol{u}$ is the neutral wind velocity, T is the plasma temperature, ν_i is the ion-neutral collision frequency, ν_e is the electron-neutral collision frequency, M_i is the ion mass, M_e is the electron mass, $\boldsymbol{E}$ is the electric field, $\boldsymbol{B}$ is the magnetic field, $\boldsymbol{g}$ is the gravitational acceleration, and e is the absolute value of the charge on an electron.

If $\boldsymbol{v}_i$ is known, Eq. (4) defines a flux-conservative initial value problem for the density n. Ion flux flows along the velocity field $\boldsymbol{v}_i$, and the corresponding change in the ion density is given by Eq. (4). When the derivatives are approximated by finite differences, Eq. (4) allows the ion density at time $t+\Delta t$ to be computed approximately from the ion density at time t. Iterating this computation gives an approximate solution for the time evolution of the ion density. The accuracy of the solution depends on the accuracy of the derivative approximations. Low order approximations introduce excessive "numerical" diffusion. Higher order approx-
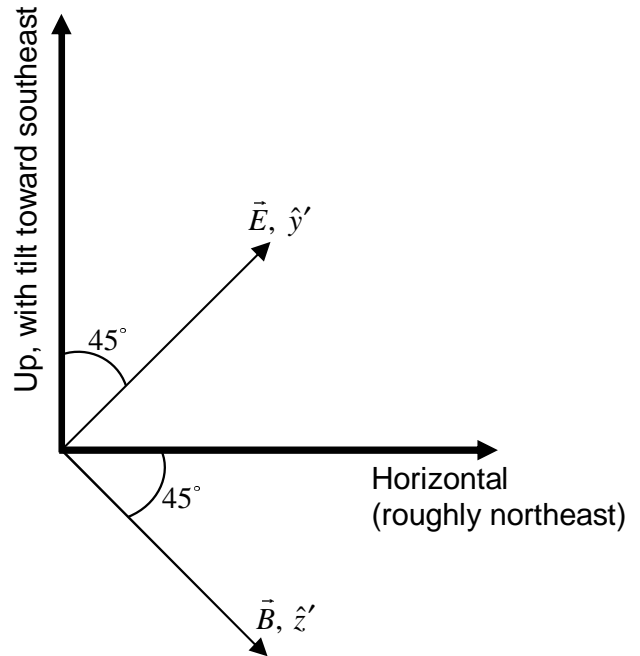

Fig. 3. Axis orientation for Fig. 4 through Fig. 12. The coordinate axes, $\boldsymbol{E}$, and $\boldsymbol{B}$, all lie in the planes of the figures.

imations are more accurate, but introduce non-physical ripples. In this paper we use a low order approximation which cannot produce any non-physical ripples.

The ion velocity for use in Eq. (4) is recomputed at each time step. The neutral wind velocity is taken to be the rotational wind field (Eq. 1). The ion-neutral collision frequency is computed from an analytical expression fit to curves given in Johnson (1961),

$$\nu_i = \nu_1 e^{(z-z_1)/H_1} + \nu_2 e^{(z-z_2)/H_2} + \nu_3 e^{(z-z_3)/H_3}, \qquad (6)$$

where for low solar activity the parameters are $\nu_1=5000\,\text{s}^{-1}$, $z_1=100\,\text{km}$, $H_1=5.5\,\text{km}$, $\nu_2=400\,\text{s}^{-1}$, $z_2=100\,\text{km}$, $H_2=16\,\text{km}$, $\nu_3=8\,\text{s}^{-1}$, $z_3=120\,\text{km}$, and $H_3=50\,\text{km}$. Working in a righthanded coordinate system with the third axis aligned with $\boldsymbol{B}$, Eqs. (2) and (3) may be solved explicitly for the ion and electron velocities as a function of $\boldsymbol{E}$:

$$\boldsymbol{v}_i = \frac{1}{M_i} \frac{\nu_i}{\nu_i^2 + \Omega_i^2} \begin{pmatrix} 1 & \frac{\Omega_i}{\nu_i} & 0 \\ \frac{-\Omega_i}{\nu_i} & 1 & 0 \\ 0 & 0 & \frac{\nu_i^2+\Omega_i^2}{\nu_i^2} \end{pmatrix} \boldsymbol{F}_i$$

$$\boldsymbol{v}_e = \frac{1}{M_e} \frac{\nu_e}{\nu_e^2 + \Omega_e^2} \begin{pmatrix} 1 & \frac{-\Omega_e}{\nu_e} & 0 \\ \frac{\Omega_e}{\nu_e} & 1 & 0 \\ 0 & 0 & \frac{\nu_e^2+\Omega_e^2}{\nu_e^2} \end{pmatrix} \boldsymbol{F}_e \text{ where}$$

$$\boldsymbol{F}_i = e\boldsymbol{E} + M_i \nu_i \boldsymbol{u} - \frac{T\nabla n}{n} + M_i \boldsymbol{g}$$

$$F_e = -eE + M_e\nu_e u - \frac{T\nabla n}{n} + M_e g$$

$$\Omega_i = \frac{eB}{M_i} \text{ and } \Omega_e = \frac{eB}{M_e}. \qquad (7)$$

Hence, E must be computed from the ion-density distribution at each time step.

The electric field E is found by solving the current continuity equation, which is obtained by subtracting Eq. (5) from Eq. (4) and multiplying by e:

$$\nabla \cdot J = \nabla \cdot [en(v_i - v_e)] = 0. \qquad (8)$$

When Eq. (7) is substituted into Eq. (8) a differential equation for E is obtained. We begin by solving Eq. (8) using the approximation that the component of E perpendicular to B maps unattenuated along B. Working in the primed coordinate system (Fig. 2), which has $\hat{z}'$ aligned with B, we integrate Eq. (8) along B:

$$\frac{\partial}{\partial x'}\int_{-z_0'}^{z_0'} dz' \, J_{x'} + \frac{\partial}{\partial y'}\int_{-z_0'}^{z_0'} dz' \, J_{y'} + J_{z'}(z_0') - J_{z'}(-z_0') = 0. \quad (9)$$

As argued in Sect. 3.1, the first term is zero, because the invariance of physical quantities along x makes field line integrated quantities invariant along x'. The field aligned current evaluated on the boundary (the last two terms) is zero by the assumption that no current exits the bottom of the E_s layer, or the top of the F layer. Hence, only the second term is nonzero, and the current continuity condition reduces to

$$\int_{-z_0'}^{z_0'} dz' \, J_{y'} = C = \text{constant}. \qquad (10)$$

The electric field may be obtained by substituting an expression for the current density as a function of E, and solving the one-dimensional Eq. (10).

The current density J is found by subtracting v_e from v_i and multiplying by en. Using Eq. (7) we find

$$\begin{pmatrix} J_{x'} \\ J_{y'} \\ J_{z'} \end{pmatrix} = n \begin{pmatrix} \sigma_P & -\sigma_H & 0 \\ \sigma_H & \sigma_P & 0 \\ 0 & 0 & \sigma_0 \end{pmatrix} \begin{pmatrix} u_{y'}B \\ E_{y'} - u_{x'}B \\ E_{z'} \end{pmatrix}$$

$$+ T \begin{pmatrix} \alpha_P & -\alpha_H & 0 \\ \alpha_H & \alpha_P & 0 \\ 0 & 0 & \alpha_0 \end{pmatrix} \begin{pmatrix} \frac{\partial n}{\partial x'} \\ \frac{\partial n}{\partial y'} \\ \frac{\partial n}{\partial z'} \end{pmatrix}$$

$$+ n \begin{pmatrix} \gamma_P & -\gamma_H & 0 \\ \gamma_H & \gamma_P & 0 \\ 0 & 0 & \gamma_0 \end{pmatrix} \begin{pmatrix} g_{x'} \\ g_{y'} \\ g_{z'} \end{pmatrix}, \quad \text{where}$$

$$\sigma_P = \frac{e}{B}\frac{\Omega_e \nu_e}{\Omega_e^2 + \nu_e^2} + \frac{e}{B}\frac{\Omega_i \nu_i}{\Omega_i^2 + \nu_i^2}$$

$$\sigma_H = \frac{e}{B}\frac{\Omega_e^2}{\Omega_e^2 + \nu_e^2} - \frac{e}{B}\frac{\Omega_i^2}{\Omega_i^2 + \nu_i^2}$$

$$\sigma_0 = \frac{e}{B}\frac{\Omega_e}{\nu_e} + \frac{e}{B}\frac{\Omega_i}{\nu_i}$$

$$\alpha_P = \frac{1}{B}\frac{\Omega_e \nu_e}{\Omega_e^2 + \nu_e^2} - \frac{1}{B}\frac{\Omega_i \nu_i}{\Omega_i^2 + \nu_i^2}$$

$$\alpha_H = \frac{1}{B}\frac{\Omega_e^2}{\Omega_e^2 + \nu_e^2} + \frac{1}{B}\frac{\Omega_i^2}{\Omega_i^2 + \nu_i^2}$$

$$\alpha_0 = \frac{1}{B}\frac{\Omega_e}{\nu_e} - \frac{1}{B}\frac{\Omega_i}{\nu_i}$$

$$\gamma_P = \frac{e\nu_i}{\nu_i^2 + \Omega_i^2} - \frac{e\nu_e}{\nu_e^2 + \Omega_e^2}$$

$$\gamma_H = -\frac{e\Omega_i}{\nu_i^2 + \Omega_i^2} - \frac{e\Omega_e}{\nu_e^2 + \Omega_e^2}$$

$$\gamma_0 = \frac{e}{\nu_i} - \frac{e}{\nu_e}. \qquad (11)$$

Substituting Eq. (11) into Eq. (10), using the approximation that the component of E perpendicular to B maps unattenuated along B ($E_{y'}$ independent of z'), and solving for $E_{y'}$ gives

$$E_{y'} = \frac{C}{\int dz' \, n\sigma_P} + \frac{B\int dz' \, n\sigma_P u_{x'}}{\int dz' \, n\sigma_P} - \frac{B\int dz' \, n\sigma_H u_{y'}}{\int dz' \, n\sigma_P}$$

$$- \frac{T\int dz' \, \alpha_H \frac{\partial n}{\partial x'}}{\int dz' \, n\sigma_P} - \frac{T\int dz' \, \alpha_P \frac{\partial n}{\partial y'}}{\int dz' \, n\sigma_P}$$

$$- \frac{g_{x'}\int dz' \, n\gamma_H}{\int dz' \, n\sigma_P} - \frac{g_{y'}\int dz' \, n\gamma_P}{\int dz' \, n\sigma_P}. \qquad (12)$$

The choice of the constant C must be made on physical grounds, and will be discussed in Sect. 3.3.

To calculate the component of E perpendicular to B ($E_{y'}$), we have assumed that the component parallel to B is negligible. This approximation is justified because the magnetic field aligned conductivity is much larger than the transverse conductivity. However, the field aligned electric field is important for certain aspects of the layer evolution, so that we don't want to assume it is zero except when computing $E_\perp$. Specifically, for a perfectly flat layer there remains an ambipolar electric field that forms because electrons have a higher mobility than ions along B, and hence diffuse faster down a gradient. The ambipolar electric field is directed away from the layer, and is a significant factor in determining the equilibrium layer thickness. The field aligned electric field $E_\parallel$ will be computed by integrating[1] the current

---

[1]A complication arises because the direction perpendicular to the simulation plane is a symmetry direction only for field line integrated quantities, so that $\frac{\partial J_{x'}}{\partial x'} \neq 0$, and it is necessary to derive $\frac{\partial J_{x'}}{\partial x'}$ in terms of $\frac{\partial J_{x'}}{\partial y'}$ and $\frac{\partial J_{x'}}{\partial z'}$. It is possible to do this because there is in fact a symmetry direction; it just doesn't happen to lie along a convenient coordinate axis. The needed geometric result is rather complex, and we will not include it here.

continuity equation to get the field aligned current $J_{z'}$ (using the perpendicular field $E_{y'}$ computed with the approximation that $E_\parallel=0$), and then solving for the $E_\parallel$ necessary to drive the current.

3.3 Boundary conditions

The local current continuity equation does not have a unique solution unless boundary conditions are specified. To establish physical boundary conditions we must consider the global current closure problem, such as was done by Cosgrove and Tsunoda (2001, 2002a). The polarization electric field, which is in the $\hat{y}'$ direction, drives Hall currents perpendicular to the simulation plane (i.e. in the $\hat{x}'$ direction). The global closure of these Hall currents is not enforced by the local current closure equation, because the invariance assumption means that the simulation domain is effectively infinite in the direction perpendicular to the simulation plane. To assure global current closure we require that these currents sum to zero over the simulation plane. Specifically, the integral along y' of the field-line-integrated Hall current due the polarization electric field is zero, $\int dy' \left[E_{y'} \int dz' \, n\sigma_H \right]=0$. Using Eq. (12) in this expression and solving for C gives

$$C = -\int dy' \left[\frac{B \int dz' \, n\sigma_H \int dz' \, n\sigma_P u_{x'}}{\int dz' \, n\sigma_P} \right] / G$$

$$+ \int dy' \left[\frac{B \int dz' \, n\sigma_H \int dz' \, n\sigma_H u_{y'}}{\int dz' \, n\sigma_P} \right] / G$$

$$+ \int dy' \left[\frac{T \int dz' \, n\sigma_H \int dz' \, \alpha_H \frac{\partial n}{\partial x'}}{\int dz' \, n\sigma_P} \right] / G$$

$$+ \int dy' \left[\frac{T \int dz' \, n\sigma_H \int dz' \, \alpha_P \frac{\partial n}{\partial y'}}{\int dz' \, n\sigma_P} \right] / G$$

$$+ \int dy' \left[\frac{g_{x'} \int dz' \, n\sigma_H \int dz' \, n\gamma_H}{\int dz' \, n\sigma_P} \right] / G$$

$$+ \int dy' \left[\frac{g_{y'} \int dz' \, n\sigma_H \int dz' \, n\gamma_P}{\int dz' \, n\sigma_P} \right] / G \quad \text{where,}$$

$$G = \int dy' \left[\frac{\int dz' \, n\sigma_H}{\int dz' \, n\sigma_P} \right]. \tag{13}$$

Note that for the unperturbed layer the integrands of the y' integrations are constants, so that cancellation occurs, and C is simply that necessary to make $E_{y'}$ in Eq. (12) equal to zero.

Periodic boundary conditions are applied to the plasma density and electric field in the horizontal grid direction. This means, for example, that $\boldsymbol{E}_\perp$ maps down $\boldsymbol{B}$ until it hits the right edge of of the simulation region, then continues from the left edge. Hence, field line integrations wrap in this way. Plasma arriving at the left or right boundaries of the grids reappears at the opposite boundary. The horizontal dimension of the simulation grids are 200 km, and the initial layers

extend the whole 200 km. Therefore, we assume that the upper limit horizontal scale of real world E_s distributions exceeds 200 km, and that any edge effects from a finite upper scale can be neglected. Plasma arriving at the top and bottom boundaries of either grid (E_s or F) is removed from the simulation space.

4 Results

The simulation results are presented in Figs. 4 through 12. The figures show cross sections of the E_s layer and F layer densities in grey scale, and the electric field at the equilibrium altitude of the E_s layer. The orientation of the coordinate axes is summarized in Fig. 3, which was described in detail in Sect. 3.1. Briefly, the axes are defined so that both $\boldsymbol{B}$ and $\boldsymbol{E}$ lie in the figure plane. The abscissa is roughly northeast, and $\boldsymbol{B}$ makes a 45° angle with it, directed from top left to bottom right. The electric field $\boldsymbol{E}$ is perpendicular to $\boldsymbol{B}$, with positive defined from bottom left to top right. The sacrifice for making $\boldsymbol{B}$ and $\boldsymbol{E}$ lie in the plane of the figure is that the ordinate is directed upward with a tilt toward the southeast. The abscissa, however, is exactly horizontal.

The exercise of transforming to a coordinate system where the ordinate is exactly altitude has been carried out for completeness. Essentially, the only effect of this transformation is to divide the coordinate components on the ordinate by (approximately) $\sqrt{2}$. We elect not to include a figure showing this rather mundane effect. Note that the electric and magnetic fields would make oblique angles with respect to the plane of such a figure.

The rotational wind field (Eq. 1) is applied in the E region. A zonal wind shear of 35 m/s/km is present at the equilibrium E_s layer altitude. A uniform wind field of 45 m/s to the east, and 22 m/s to the south, is applied in the F region. There is no background (i.e., not caused by polarization of the E_s layer) electric field. A 0.6 km half width Gaussian density profile is located at its' equilibrium altitude (at the zero of the zonal wind) on the E region grid, and a 120 km half width Gaussian density profile is located at its' equilibrium altitude (where gravity is balanced by wind) on the F region grid. Depending on the relative peak densities of the layers, and on the equilibrium altitudes, which will be simulation parameters, the configuration described is unstable to both the Perkins and E_s layer instabilities.

The equivalence between winds and electric fields can be used to generalize the simulation results to other conditions, for example, inclusion of meridional electric fields. The "effective" electric field is $\boldsymbol{E}'=\boldsymbol{E}+\boldsymbol{u}\times\boldsymbol{B}$, where $\boldsymbol{u}$ is the neutral wind velocity. As long as the effective electric field in the F layer, the effective electric field in the E_s layer, and the shear in effective electric field at the E_s layer altitude (and in proximity thereof) are the same, then the simulation results will be the same, up to an overall horizontal velocity offset. (This
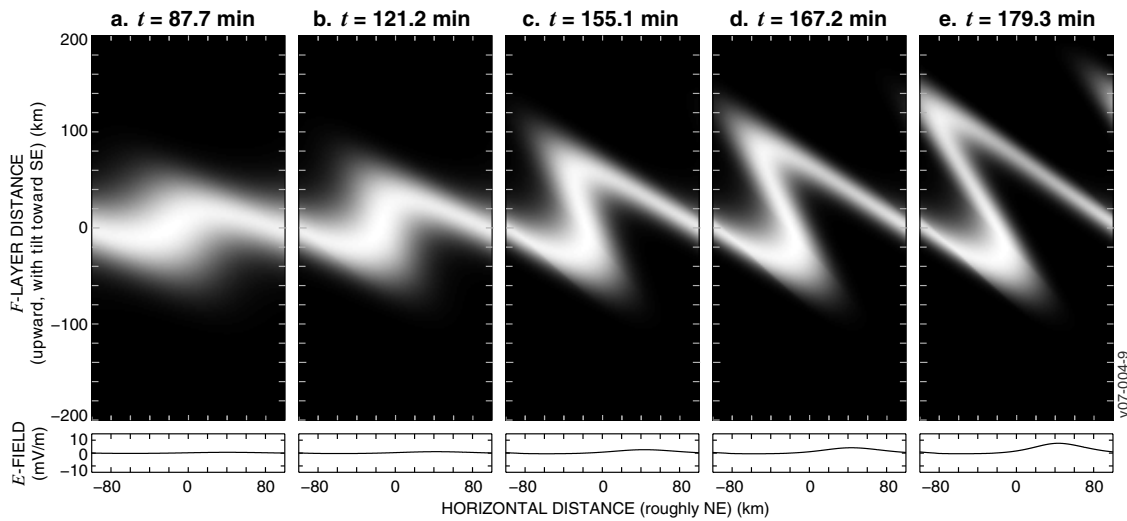
Fig. 4. F layer evolution with no E_s layer present (Perkins Instability), for a 200 km wavelength initial seed. The boundary conditions are periodic in the horizontal direction. The axes are described in the first paragraph of Sect. 4, and summarized in Fig. 3.

follows under the assumption that $\boldsymbol{E}$ maps along $\boldsymbol{B}$, and that all winds are horizontal.)

Table 1 shows the remaining parameters for the simulations in each figure. The second column contains the ratio Σ_H/Σ_{PF} of the FLI Hall conductivity of the E_s layer to the FLI Pedersen conductivity of the F layer. The third column contains the altitude of the E_s layer. Given the ion-neutral collision frequency as a function of altitude (Eq. 6), the ratio Σ_{PE}/Σ_{PF} of the FLI Pedersen conductivity of the E_s layer to the FLI Pedersen conductivity of the F layer can be computed from Σ_H/Σ_{PF} and the E_s layer altitude. The fourth column contains the parameter $\boldsymbol{E}' \cdot \hat{e}$, which is the eastward component of the effective electric field at the altitude of the E_s layer.

Simulations are presented for both the resonant ($\boldsymbol{E}' \cdot \hat{e}=0$) and non-resonant ($\boldsymbol{E}' \cdot \hat{e} \gg 0$) cases. (See Sect. 2 for an explanation of the parameter $\boldsymbol{E}' \cdot \hat{e}$.) The resonant case is achieved by setting $u_N=0$ in Eq. (1). The non-resonant case is achieved by setting $u_N=-120$ m/s in Eq. (1), which places a 120 m/s southward wind in the E_s layer, resulting in $\boldsymbol{E}' \cdot \hat{e}=5.3$ mV/m.

When no meridional electric fields are present, the E_s layer equilibrium altitude is at the zero of the zonal wind, with a westward wind above and an eastward wind below (Hines, 1974). For the rotational tidal wind profile modeled by Rosenberg (1968), based on theory described by Hines (1965) and 70 midlatitude wind profiles, this places the E_s layer in a southward wind (in the Northern Hemisphere). This configuration was also observed during the SEEK-1 rocket campaign (Fukao et al., 1998; Yamamoto et al., 1998; Larsen et al., 1998). As argued below, the southward wind leads to southwestward propagation of frontal structures in

the E_s layer. On the other hand, the sense of the tidal rotation can sometimes be reversed (Smith, 1972), which would place the E_s layer in a northward wind. A northward wind would result in northeastward propagation of frontal structures. A background northward (southward) electric field would raise (lower) the equilibrium altitude of the E_s layer relative to the wind shear, resulting in a westward (eastward) wind component in the E_s layer, with an attendant southwestward (northeastward) drift of the frontal structures. Similar considerations apply in the Southern Hemisphere, where the instability theory predicts (and observations support (Goodwin and Summers, 1970)) structures elongated from southwest to northeast.

Three values have been chosen for the ratio Σ_H/Σ_{PF}: $\Sigma_H/\Sigma_{PF}=0.5$, $\Sigma_H/\Sigma_{PF}=1.0$, and $\Sigma_H/\Sigma_{PF}=3.0$. Harper and Walker (1977) used 16 nights of Arecibo data to compute a mean nighttime time-profile for Σ_H/Σ_{PF}. The mean taken over this mean-profile is approximately $\Sigma_H/\Sigma_{PF}=2$, and the maximum approximately $\Sigma_H/\Sigma_{PF}=4$, where the maximum occurred just before midnight. It should be noted that Harper and Walker (1977) did not screen for the presence or absence of E_s layers, and emphasized that there were large fluctuations about the mean profile.

As a second way to evaluate our choices for the ratio Σ_H/Σ_{PF}, we appeal to the International Reference Ionosphere (IRI) (Bilitza, 1990) and COSPAR International Reference Atmosphere (CIRA) (Rees, 1988) models to compute the integrated Pedersen conductivity over an altitude range from 100 km to 1000 km, for various model parameters, and assign it to Σ_{PF}. To do this we use the web cite maintained by the World Data Center, Kyoto, which outputs the integrated conductivity as a function of season, sunspot number,
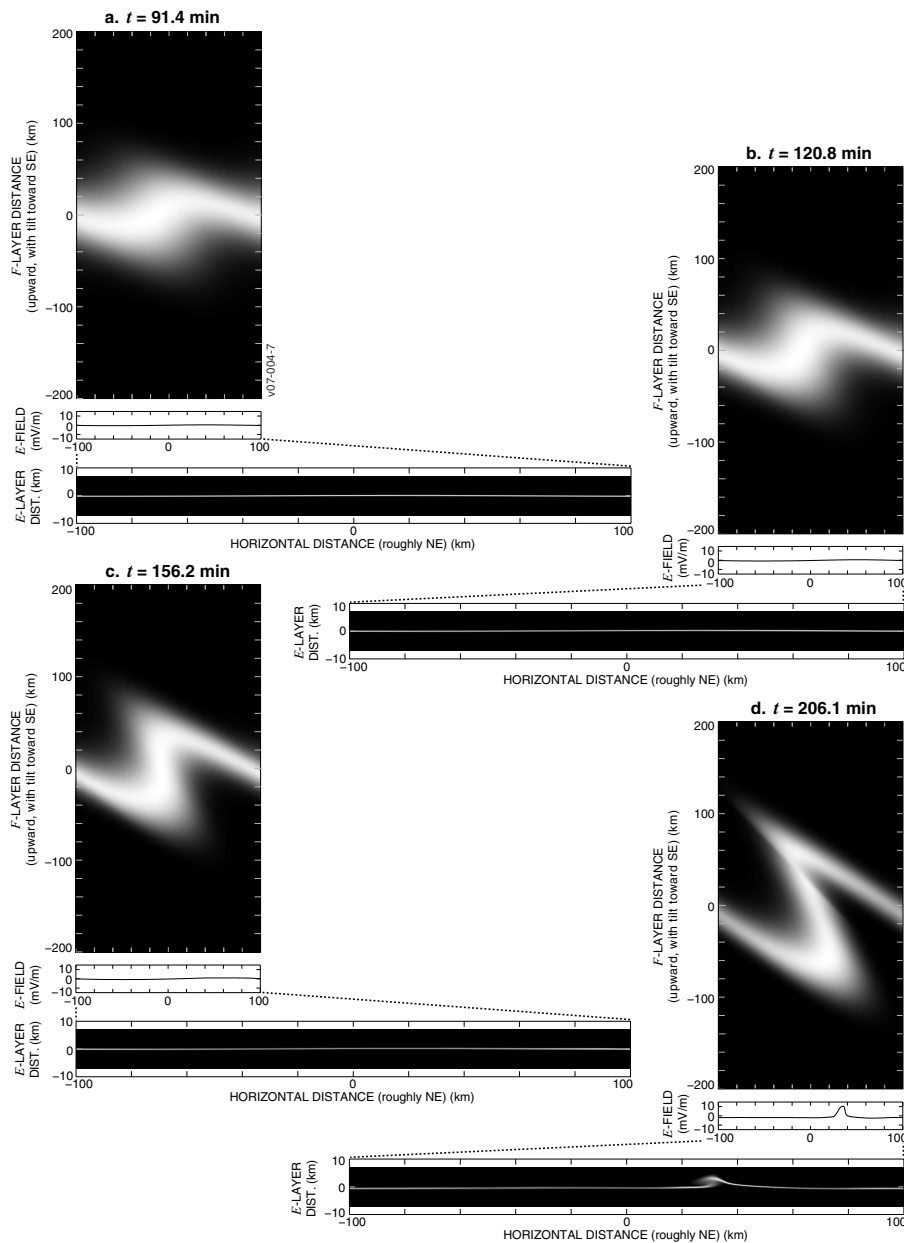
Fig. 5. Coupled system evolution under non-resonant condition, with $\frac{\Sigma_H}{\Sigma_{PF}}=0.5$, and the E_s layer at 105 km altitude. The boundary conditions are periodic in the horizontal direction. The axes are described in the first paragraphs of Sect. 4, and summarized in Fig. 3.

latitude, longitude, etc. For the E_s layer integrated conductivity we assume a 1 km thick layer with a density of $10^{11}\,\mathrm{m}^{-3}$, which gives an FLI density of $10^{14}\,\mathrm{m}^{-2}$. This choice is motivated by Figs. 7 and 8 from Miller and Smith (1978), who compiled E_s layer statistics from high resolution incoherent scatter measurements made by the Arecibo observatory. In addition, Wakabayashi et al. (2005) computed the TEC from impedance probe measurements made during the SEEK2 rocket campaign, and found values exceeding $10^{14}\,\mathrm{m}^{-2}$ for both rockets. The results for the loca-

tion of the Arecibo Observatory, and the Mu Radar in Japan, are shown in Table 2.

The reader is invited to examine Table 2 and make their own conclusions with respect to the reasonableness of the ratios $\Sigma_H/\Sigma_{PF}=1/2$, $\Sigma_H/\Sigma_{PF}=1$, and $\Sigma_H/\Sigma_{PF}=3$, chosen for the simulations. The F region conductivity is reduced in the wintertime, as seen in Table 2. On the other hand E_s layer occurrence shows a statistical preference for summertime (e.g., Whitehead, 1989). Hence, if the ratio Σ_H/Σ_{PF} is in fact important, it is perhaps not surprising that MSTID

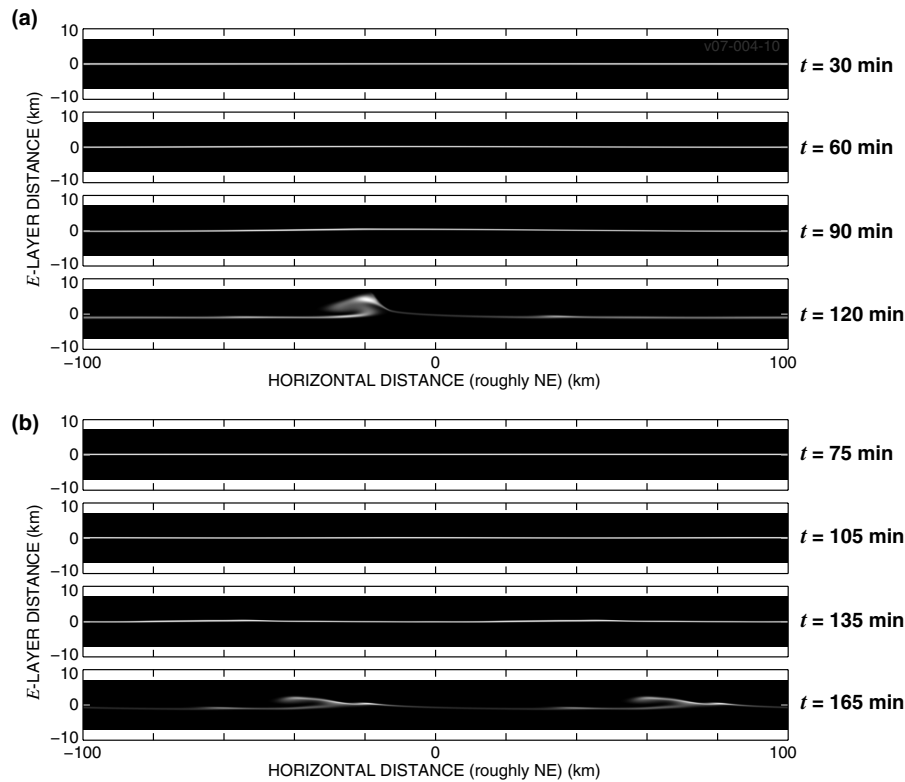**Fig. 6.** E_s layer evolution on a long time scale under the non-resonant condition, for a 200 km wavelength initial seed **(a)**, and for a 100 km wavelength initial seed **(b)**. The boundary conditions are periodic in the horizontal direction. The axes are described in the first paragraph of Sect. 4, and summarized in Fig. 3.

Table 1. Simulation parameters and purposes indexed by figure number.

	$\frac{\Sigma_H}{\Sigma_{PF}}$	E_s altitude (km)	$E' \cdot \hat{e}$ (mV/m)	Comment
Fig. 4	0	NA	NA	Perkins instability.
Fig. 5	0.5	105	5.3	Nearly negligible E_s.
Fig. 6	1.0	105	5.3	E_s on long time scale, for two wavelengths.
Fig. 7	1.0	105	5.3	Linear stage of E_s layer instability.
Fig. 8	1.0	105	0	E_s eruption under resonant condition.
Fig. 9	1.0	105	0	After E_s eruption under resonant condition.
Fig. 10	1.0	105	5.3	E_s eruption under nonresonant condition.
Fig. 11	1.0	105	5.3	After E_s eruption under nonresonant condition.
Fig. 12	3.0	103	5.3	E_s eruption with dense layer.

statistics are not simple. Shiokawa (2003) found an MSTID occurrence maximum in summertime, in the Japanese sector, while Garcia et al. (2000) found an MSTID occurrence minimum in the summertime, over the Arecibo observatory in Puerto Rico. Finally, to assess the reasonableness of the conductivity ratios chosen for the simulation, we should keep in mind that Harper and Walker (1977) observed large fluctuations of the F region integrated conductivity about its mean.

Hence, in order to consider an uncommon event, like that observed by Behnke (1979), we should consider conductivity ratios far from the mean.

Throughout, we have seeded the simulations with a ± 5 km amplitude, 200 km wavelength altitude modulation of the F layer. The initial E_s layer is horizontally uniform. We choose this initial configuration because the amplitude of gravity waves grows with altitude. The amplitude of 200 km

Table 2. $\frac{\Sigma_H}{\Sigma_{PF}}$ ratio computed from IRI/CIRA models for the F layer conductivity, at 23:00 LT, and an E_s layer based on Miller and Smith (1978).

$\frac{\Sigma_H}{\Sigma_{PF}}$	Σ_{PF} from IRI/CIRA (mhos)	Sunspot #	Month	Location
1.2	0.303	10	July	Arecibo Observatory
0.2	2.351	110	July	Arecibo Observatory
3.0	0.119	10	Jan	Arecibo Observatory
0.3	1.340	110	Jan	Arecibo Observatory
1.5	0.241	10	July	MU Radar
0.3	1.282	110	July	MU Radar
5.9	0.061	10	Jan	MU Radar
0.9	0.409	110	Jan	MU Radar

horizontal wavelength gravity waves is thought to be quite small in the E region, but can become significant in the F region. Therefore, F region seeding seems more plausible at long wavelengths. Shorter wavelength gravity waves may be effective at seeding the E_s layer instability directly, but we do not consider this effect here.

We will organize a discussion of our findings around Figs. 4 through 12.

4.1 Figures 4 and 5: Perkins instability without an E_s layer, and least dense E_s layer case

Figure 4 shows the F layer evolution when no E_s layer is present. After about 2 h a noticeable modulation of the F layer is present. After 3 h the modulation has become extremely large. The electric field remains small throughout most of the evolution, although it begins to increase in the later stages when the altitude modulation becomes very large, eventually reaching 7 mV/m. The structure does not exhibit translation, due to the fact that the background electric field is zero. Continuing to run the simulation causes the altitude peak to exit the simulation grid.

Figure 5 shows the coupled system evolution with an E_s layer present such that $\Sigma_H/\Sigma_{PF}=0.5$, under the non-resonant condition. For the first 2.5 h the F layer evolution remains essentially the same. However, the altitude modulation of the F layer is noticeably limited thereafter, and a breaking wave is eventually observed in the E_s layer, with an associated 10 mV/m electric field pulse, about 10 km in horizontal extent. At $t=206$ min the F layer modulation equals that at $t=167$ min without an E_s layer, whereas (without an E_s layer at $t=206$ min) the F layer would have exited the simulation grid. Hence, the disturbing effect of the E_s layer electrodynamics appears to cause saturation of the growth of the F layer modulation. Under the resonant condition (not shown) an E_s layer with $\Sigma_H/\Sigma_{PF}=0.5$ increases the growth rate of the F layer modulation; we will study this effect in Sect. 4.3 for the case $\Sigma_H/\Sigma_{PF}=1.0$.
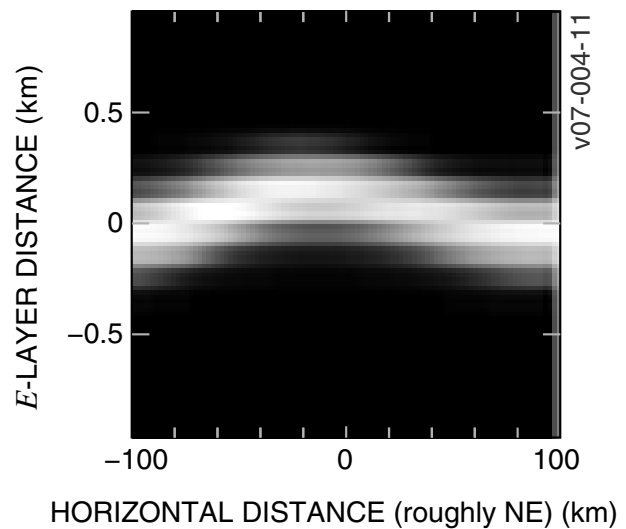

Fig. 7. The $t=60$ min panel of Fig. 6a with the ordinate scale magnified 100 times, showing the E_s layer evolution in the linear regime. The boundary conditions are periodic in the horizontal direction.

4.2 Figures 6 and 7: F-layer seeded E_s instability on long time scale, including the linear regime

Figure 6 shows the E_s layer evolution on a long time scale, with $\Sigma_H/\Sigma_{PF}=1$, under the non-resonant condition, for a 200 km wavelength initial seed in panel (a), and for a 100 km wavelength initial seed in panel (b). For most of the period of evolution the changes in the E_s layer are subtle. This relatively long "preparatory" phase of evolution is followed by an explosive phase, when the E_s layer evolution becomes strongly nonlinear, taking the form of a breaking wave (as already seen in Fig. 5). Figure 7 shows a view of the $t=60$ min profile of Fig. 6 that has been stretched along the ordinate by a factor of 100. With this extreme stretching it is possible to see the 200 km wavelength sinusoidal altitude modulation
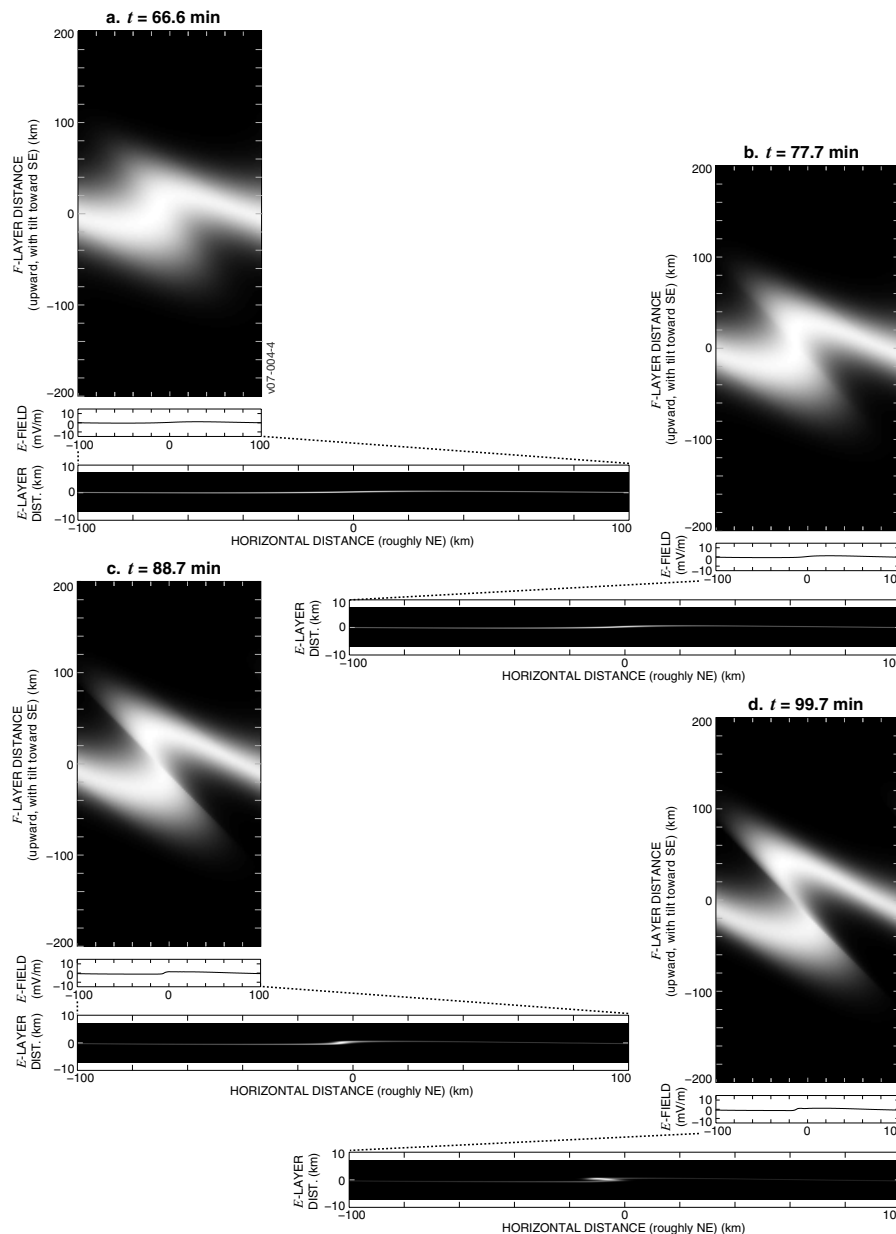
Fig. 8. Coupled system evolution under resonant condition, with $\frac{\Sigma_H}{\Sigma_{PF}}=1.0$, and the E_s layer at 105 km altitude. The boundary conditions are periodic in the horizontal direction. The axes are described in the first paragraphs of Sect. 4, and summarized in Fig. 3.

present in the linear stage of the E_s layer instability growth. This preparatory phase of evolution would probably be unobservable, using standard E_s layer observing techniques (e.g., ionosonde), so that the system would appear to evolve on short time and spatial scales. The spatial scale would appear much less than 200 km.

Recall that the seed for the instabilities was given in the F region. It takes some time for the Perkins instability to evolve, and for the F region polarization fields to increase sufficiently to affect the E_s layer. Because the E_s layer is so

much thinner, applying a seed directly to the E_s layer could produce an effect much more quickly, even if the seed were quite small. However, the spectrum of gravity waves in the E region is thought to be dominated by shorter wavelengths, and hence we assume that direct seeding of the E_s layer instability would occur only at shorter wavelengths. Because of our modeling decision to place the seed in the F region, it takes a relatively long time for structures to develop.

Because we employ periodic boundary conditions in the horizontal direction, Fig. 6a represents a structure with a
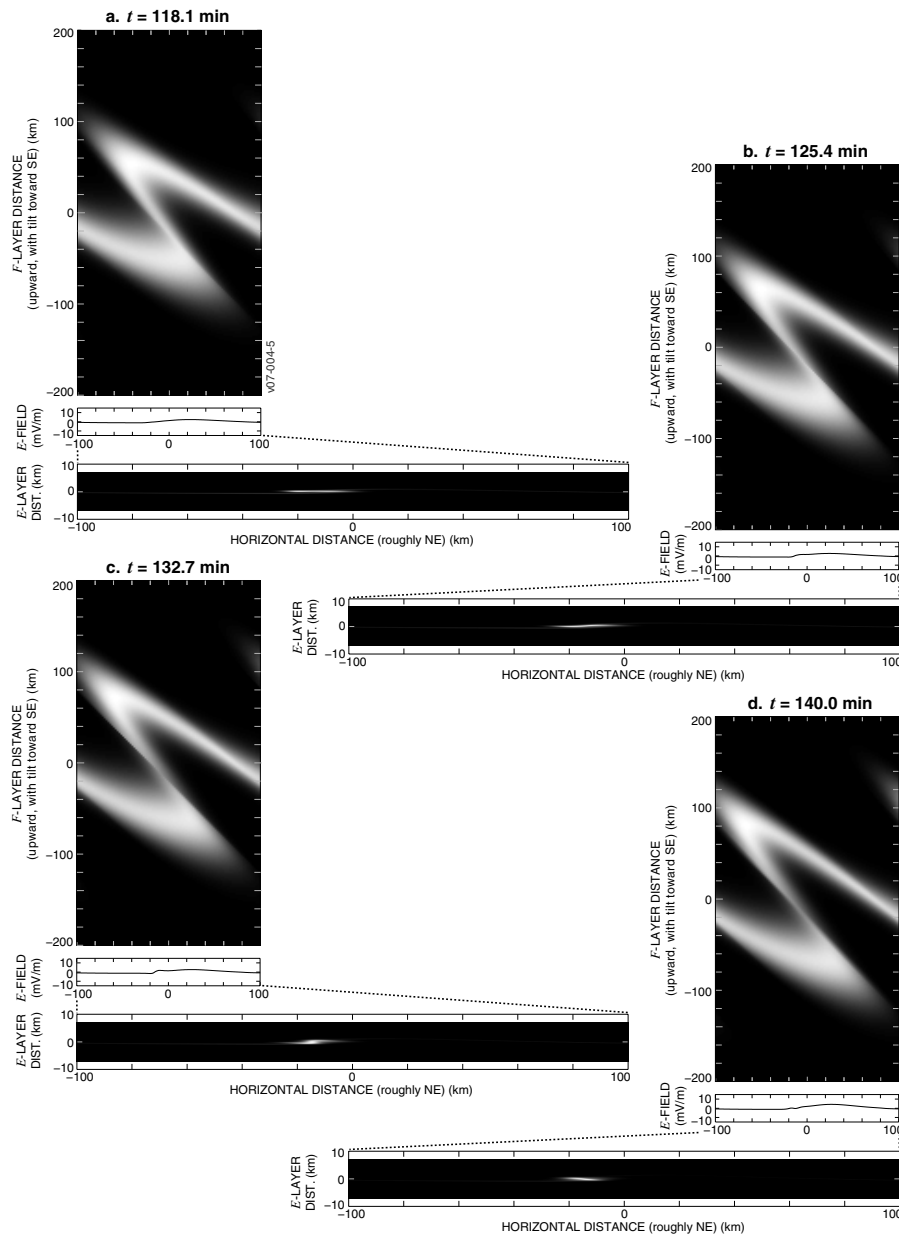
Fig. 9. Continuation of the simulation in Fig. 8.

200 km horizontal periodicity. Figure 6a results from a 200 km initial seed perturbation. Using instead a 100 km initial seed perturbation results in Fig. 6b, which displays a 100 km periodicity throughout the whole evolution period. From this we conclude that a 200 km simulation domain is sufficient to model the evolution resulting from a 200 km initial seed. Using a 400 km domain would only result in the display of two copies of the same structure, etc.

4.3 Figures 8 and 9: resonant condition for mid-range conductivity ratio

Figure 8 shows the coupled system evolution with $\Sigma_H/\Sigma_{PF}{=}1.0$, under the resonant condition. Over a 10 min interval an initially slightly tilted region of dense plasma in the E_s layer steepens and then breaks like an ocean wave. A mild 1 or 2 mV/m electric field peaks when the wave breaks. The majority of the F layer modulation is synchronized with the event.
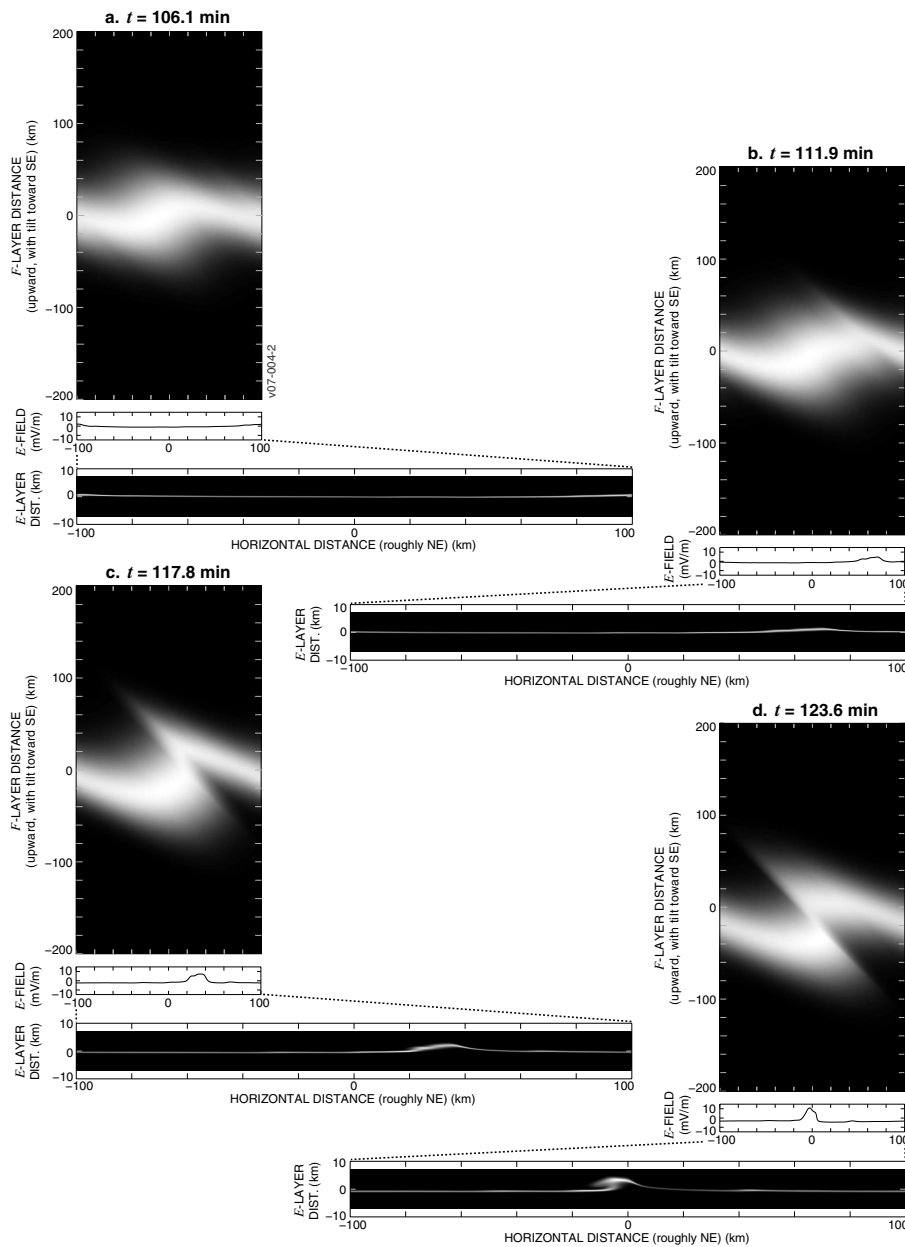
Fig. 10. Coupled system evolution under non-resonant condition, with $\frac{\Sigma_H}{\Sigma_{PF}}=1.0$, and the E_s layer at 105 km altitude. The boundary conditions are periodic in the horizontal direction. The axes are described in the first paragraphs of Sect. 4, and summarized in Fig. 3.

In Fig. 9 the evolution after the wave breaking event in Fig. 8 is shown. There appears to be a second wave breaking event in the E_s layer, after which the plasma is left gathered into a localized dense region. In contrast to the E_s layer, the modulation of the F layer continues to grow with almost no distortion from a pure sinusoid.

In summary, in the resonant case the E_s layer provides an initial kick to the F layer, but then goes highly nonlinear, at which point the Perkins instability takes over. The initial modulation of the F layer altitude is achieved in about one half the time as when no E_s layer is present.

4.4 Figures 10 and 11: non-resonant condition for mid-range conductivity ratio

We turn now to comparing the resonant condition ($E'\cdot\hat{e}=0$) to the non-resonant condition ($E'\cdot\hat{e}\gg0$). Note that the non-resonant condition should be more common in nature, since it does not require the coincidental condition $E'\cdot\hat{e}\sim0$. Figures 10 and 11 show simulations with the same conditions as Figs. 8 and 9, except with $E'\cdot\hat{e}=5.3$ mV/m. It is evident that the breaking wave in Fig. 10 has a greater altitude extent than in Fig. 8, and that the accompanying electric field
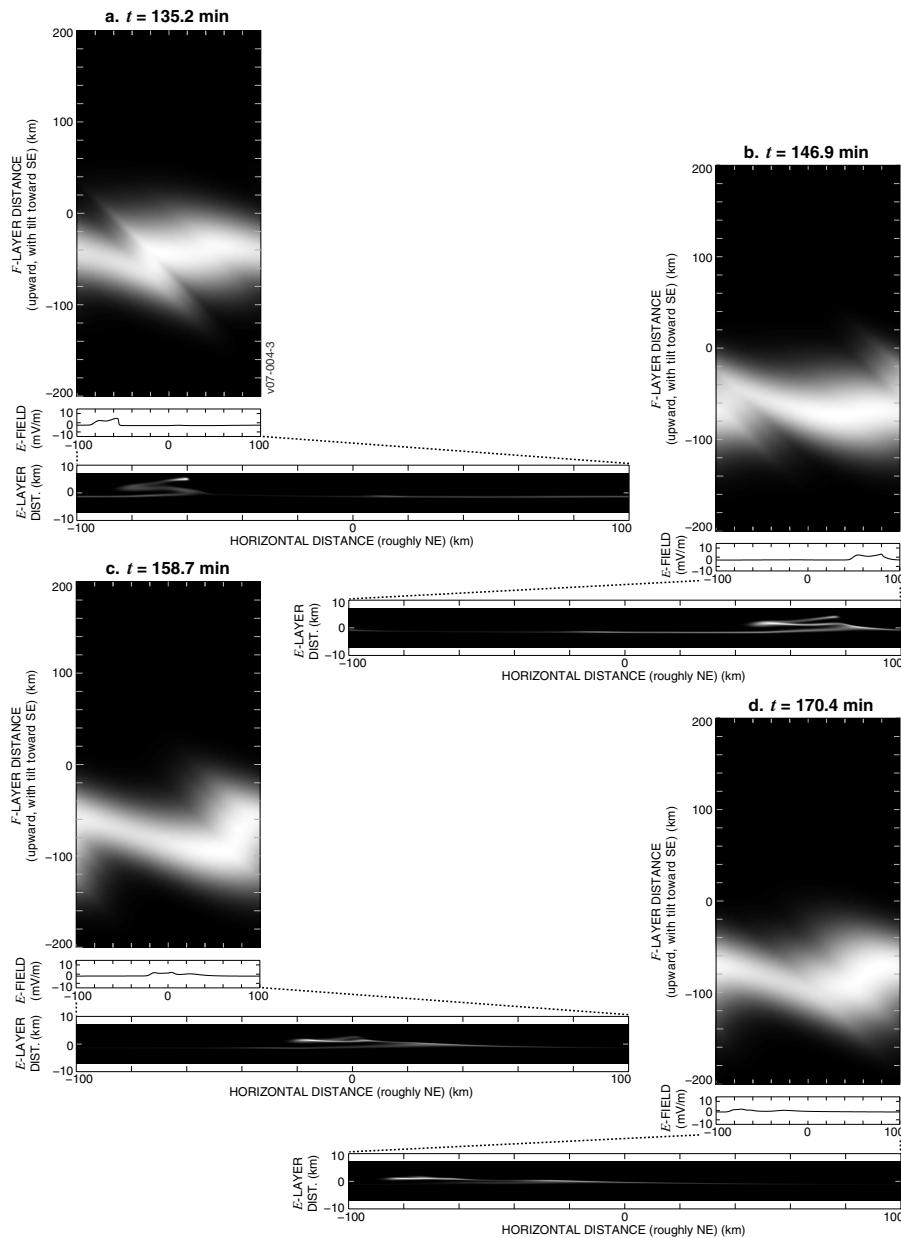
Fig. 11. Continuation of the simulation in Fig. 10.

is much larger. There is a localized 10 mV/m electric field spike in the non-resonant case, which is five times larger than the electric field in the resonant case. However, in spite of this much larger electric field, the F layer altitude modulation is less dramatic. This is explained by the fact that the E_s layer and the F layer have a relative velocity of $E' \cdot \hat{e}/B \simeq .0053/.000044 = 120$ m/s $= 432$ km/h, so that there is only a limited amount of time for the F layer plasma to react before it moves away from the localized strong electric field.

In the period after the breaking wave, shown in Fig. 11, the F layer altitude modulation does not continue to grow, as in the resonant case. Instead the F layer is flattened back out, and the whole layer pulled downward from its original altitude. It appears that the E_s layer generated electric field moves out of phase with the initial F layer altitude modulation it caused, so that it acts to undo the modulation. In the panel at t=158.7 min the altitude modulation appears again, indicating that the electric field may have moved back in phase. The overall lowering of the F layer is a result of the nonsinusoidal electric field waveform, which is caused
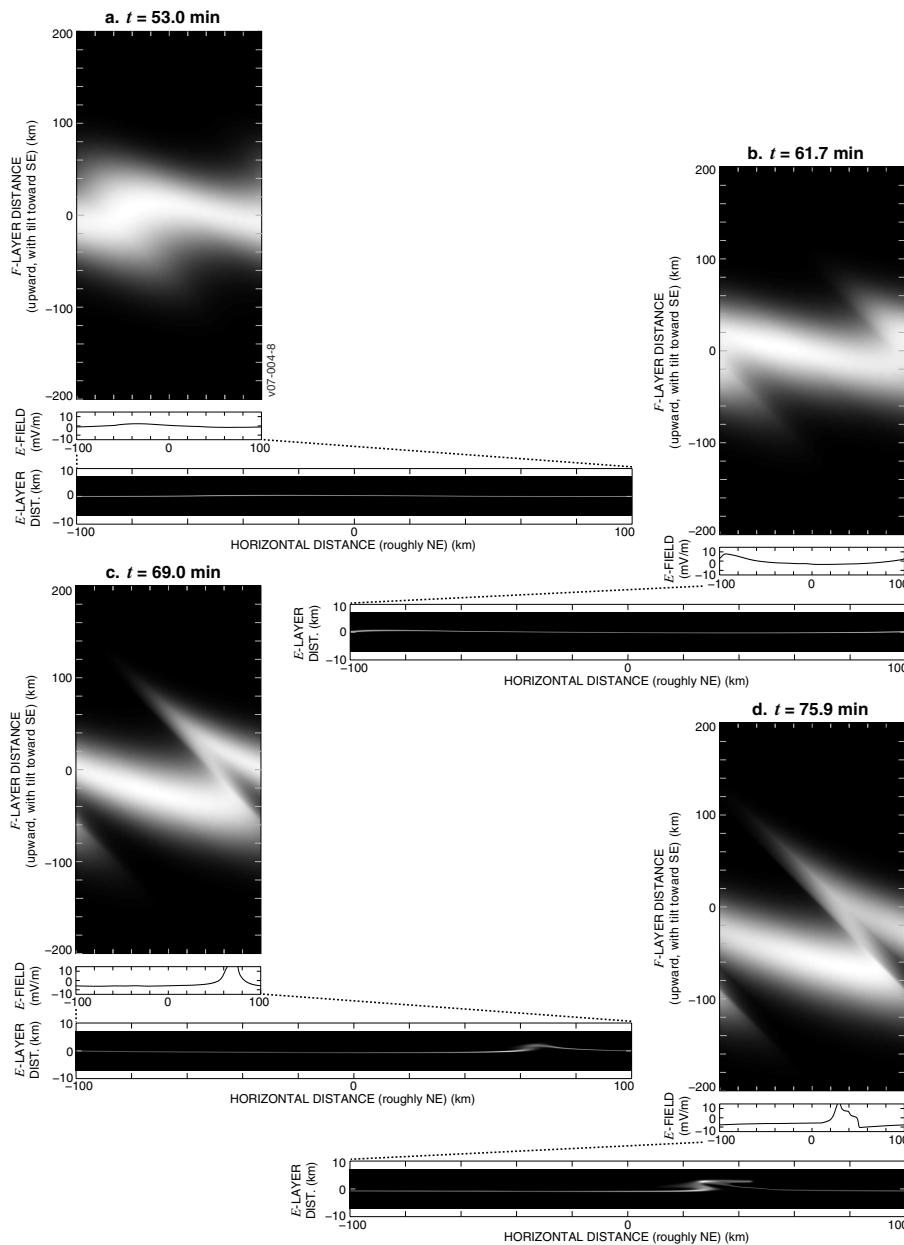
Fig. 12. Coupled system evolution under non-resonant condition, with $\frac{\Sigma_H}{\Sigma_{PF}} = 3.0$, and the E_s layer at 103 km altitude. The boundary conditions are periodic in the horizontal direction. The axes are described in the first paragraphs of Sect. 4, and summarized in Fig. 3.

by the highly nonlinear E_s layer evolution. Note that this lowering increases the F layer FLI conductivity, and hence acts to quench the E_s layer instability. There is no sign of a second E_s layer eruption. Instead of gathering together, as in the resonant case, the E_s layer remains spread out, and in some areas appears as a double, and even triple layer.

The larger electric field pulse, and the different character of the evolution in the non-resonant case is due to the fact that $E' \cdot \hat{e}$ acts to couple E_s layer altitude modulations (which modulate the wind in the layer, due to the wind shear) with E_s layer FLI density modulations (Cosgrove and Tsun-

oda, 2002b, 2003, 2007). $E' \cdot \hat{e}$ drives a zeroth order Hall current through the E_s layer, so that modulation of the FLI density (which modulates the FLI conductivity) creates polarization electric fields, in order to maintain current continuity. The bunched up E_s layer seen in Fig. 9a (resonant case) would lead to a very large polarization electric field if $E' \cdot \hat{e} = 5.3$ mV/m. Hence, it appears that such bunched up structures are prevented from forming by the generation of larger E_s layer polarization electric fields, in the non-resonant case.

The Perkins instability is not in evidence in Figs. 10 and 11. Apparently, the polarization electric fields associated with the E_s layer instability when $E' \cdot \hat{e} = 5.3$ mV/m, and the drift of the electric fields with respect to the F layer (also because $E' \cdot \hat{e} \neq 0$) act to disrupt the Perkins instability.

However, the Perkins instability still plays the role of amplifying the initial F-region altitude modulation, until it is large enough to seed the instability in the moving E_s layer, through polarization electric fields that are mapped downward. The ± 5 km F-layer altitude modulation is not sufficient. Note also that a larger initial perturbation of the F layer, or a direct perturbation of the E_s layer, would cause the E_s event to happen earlier.

4.5 Figure 12: non-resonant condition for largest conductivity ratio

As our final example, we consider in Fig. 12 the effect of increasing Σ_H / Σ_{PF} from 1.0 to 3.0, for the non-resonant simulation shown in Fig. 10. The E_s eruption extends above the region of southward wind, so that some of the plasma is left behind the general southward flow. (This was also apparent in Fig. 11.) The electric field associated with the eruption exceeds 15 mV/m over a 15 km region, and an oppositely directed electric field of 7 to 11 mV/m extends over 150 km, in the region away from the eruption. In spite of the fact that this is a non-resonant case, the modulation of the F layer altitude is nearly 100 km.

In both of the non-resonant simulations we have realized $E' \cdot \hat{e} = 5.3$ mV/m by placing a 120 m/s southward wind in the E region. The tidal wind shear in the E region is rotational, and under the standard rotational configuration (Rosenberg, 1968) the E_s layer should be located at the zero of the zonal wind, in the region of southward wind. The E_s eruption, which is extended in the northwest to southeast direction, then has a phase velocity toward the southwest (to the left), as is seen in the simulations in Figs. 10, 11, and 12. Although the F layer plasma has no horizontal velocity (it is supported by winds), there is evidence that a southwestward trace velocity might show up in all sky images. This effect is most evident in Fig. 11 where the structure, although changing with time, appears to have a general leftward motion. From Fig. 11 we estimate an apparent southwestward velocity of 40 m/s.

The southwestward trace velocity provides a possible explanation for the paradox noted by Garcia et al. (2000), that the $E \times B$ drift of the F region should generally give rise to propagation of Perkins instability modes toward the northeast, whereas the observations normally indicate southwestward drifts. This explanation is an alternative to that proposed by Kelley and Makela (2001). Note, $E = 0$ in our simulation, so that the Perkins instability modes have essentially zero phase velocity. More generally, our result should be interpreted as a velocity relative to the F layer velocity. It was explained at the beginning of this section how to generalize the results to conditions including a background electric field, which would mean a nonzero velocity for the Perkins instability modes.

The features in Fig. 12 match closely the observations described by Behnke (1979), specifically the 17 mV/m electric field, the 80 km altitude modulation, the northwest to southeast elongation of the structure, and the 50 m/s southwestward propagation velocity. The Perkins instability simulations in Fig. 4 can explain the altitude modulation and the northwest to southeast alignment, but do not seem able to explain the large electric field, or the southwestward propagation.

5 Summary and conclusions

We have simulated the mesoscale electrodynamics for a two layer E_s-F system, under the assumption that electric fields with horizontal scale sizes greater than ten kilometers map unattenuated between the E_s and F layers. The following bulleted items summarize the simulation outcomes:

1. For the simulation parameters chosen herein, the Perkins instability alone ($\Sigma_H = 0$) creates structures in the F region after about two hours, with attendant electric fields of 1 or 2 mV/m. The structures drift with the background $E \times B$ velocity. Extremely large altitude modulations, exceeding 100 km, are present after about 3 h, at which time the polarization electric field reaches 7 mV/m.

2. When an E_s layer is placed in the system with no horizontal velocity relative to the F layer (resonant condition, $E' \cdot \hat{e} = 0$) the growth rate of F-layer structure is increased due to positive dynamical coupling between the E_s layer and Perkins instabilities. There is an extremely nonlinear E_s layer response that involves the breaking of a wave, resembling an ocean wave. Associated with the wave breaking are polarization electric fields of a few mV/m that provide an impulsive "kick start" for the Perkins instability. Essentially, the F layer evolution is that of the Perkins instability, but on a shorter time scale.

3. The equilibrium condition involving a large horizontal velocity between the E_s and F layers (non-resonant condition) is equivalent to the condition of a large meridional Hall current in the E_s layer. The current polarizes FLI density modulations of the E_s layer, which significantly increases the polarization electric fields associated with the E_s layer instability. As compared with the resonant case under similar conditions, the polarization electric fields associated with wave breaking are increased by a factor of five.

4. Because of the large relative horizontal velocity, the electric fields no longer work in harmony with the Perkins instability, and can disrupt it, and in some

cases dominate it. For a relative horizontal velocity of 120 m/s, the behavior as a function of $\frac{\Sigma_H}{\Sigma_{PF}}$ is categorized in bullets 5−8.

5. When $\frac{\Sigma_H}{\Sigma_{PF}}=0.5$ the E_s layer has little effect on the early stages evolution of the Perkins instability. However, once the F layer has suffered substantial modulation, electrodynamic effects in the E_s layer act to saturate the Perkins instability. These electrodynamics eventually (after the F layer is modulated 100 km in altitude) include a wave breaking event, and a 10 km wide 10 mV/m electric field pulse.

6. When $\frac{\Sigma_H}{\Sigma_{PF}} \overset{\sim}{>} 1$ there is sufficient electrodynamic activity in the E_s layer to completely change the F layer dynamics. Wave breaking events with associated large polarization electric fields ($\sim$10 mV/m) occur before there is any significant F layer modulation. Subsequent F layer altitude modulation appears to be caused by these E_s-layer-generated electric fields, and not by the Perkins instability. The F layer modulation is more transient in nature, is less sinusoidal, and less extreme (in terms of altitude extent) than in the absence of an E_s layer. After the wave breaking event a spectrum of E_s-layer-generated electric fields acts to lower the F layer altitude.

7. In the most extreme case we found a 15 mV/m electric field extending over 15 km associated with wave breaking. This event also included oppositely directed electric fields of 7 to 11 mV/m extending over 150 km.

8. Based on the common tidal wind profile, as explained in Sect. 4, a southward wind is expected at the E_s layer altitude, when the background electric field is small ($\overset{<}{\sim}$1 mV/m). Because the growing modes of the E_s layer instability have phase fronts extended northwest to southeast, the southward wind creates a southwestward wave vector. The southwestward propagation of E_s layer electric fields can lead to a southwestward trace velocity in the F layer plasma distortions, as seen especially in Fig. 11. A southwestward or westward wind at the E_s layer equilibrium altitude would have a similar effect, and should occur when there is a northward component to the background electric field, because such raises the E_s layer equilibrium altitude relative to the wind shear profile.

9. After the breaking of a wave the simple uniform E_s layer geometry no longer exists. In the non-resonant case double (and even triple) layers may form, and it takes some time before the conditions for instability are met again. In the resonant case the plasma gathers into a localized dense region, so that there is a large FLI density modulation, and the instability may be present on a smaller horizontal scale. Apparently, the FLI density

modulation is larger in the resonant case because there is no zeroth order current present to polarize it.

10. In all cases the F layer motion is essentially incompressible $\boldsymbol{E} \times \boldsymbol{B}$ drift, and no significant modulation of the FLI density occurs (at most $\pm$5%). However, the height integrated conductivity is strongly modulated ($\pm$40%–$\pm$60%).

As with any simulation of time evolution, the relevance of the results depends on the likelihood of the initial conditions. Our choices for the ratio Σ_H/Σ_{PF} are based on the observations of Harper and Walker (1977), as described in Sect. 4. We have also evaluated the selection using F region conductivities calculated using the IRI and CIRA models, together with E_s layer observations by Miller and Smith (1978), and by Wakabayashi et al. (2005). With regard to the 120 m/s southward wind and the wind shear, Larsen (2002) has examined a large set of midlatitude chemical tracer experiments, and reports that the wind speed maximum in the 100 to 110 km range exceeds 100 m/s in over 60% of the cases, and that large wind shears are common. That the horizontal spatial spectrum of E_s distributions covers the mesoscale range is evidenced by the satellite born sounder experiment described by Cathey (1969) (see Fig. 1), and the spaced ionosonde experiment of Goodwin (1966). In addition, Kelley et al. (2000), and Kelley and Makela (2001), have observed that a north or northwestward turning of the electric field is associated with MSTIDs, which may indicate that the resonance condition is relevant.

There are, however, reasons why the conditions simulated may not always accompany a E_s layer. The resonant condition $E' \cdot \hat{e} \simeq 0$ should probably be regarded as occurring only occasionally, and for a limited time duration. The horizontal extent of the wind shear region has not been measured. We have speculated that the existence of E_s layers with large horizontal extent indicates that the wind shear also has a large horizontal extent. This is consistent with the idea that the wind shear is associated with a tidal mode. However, this assumption could be defeated if the strong wind shear region were intermittent and local, so that different parts of the layer were formed at different times. Finally, E_s layers are known to posses structure on scales well below the mesoscale, and the effects of such structure have not been incorporated in the simulations.

The most important simulation parameter is $\frac{\Sigma_H}{\Sigma_{PF}}$. To determine if E_s layers really do impact F region dynamics we should study experimentally the statistics of E_s layer height integrated density. In particular, because of all the structure in E_s, the morphology of the horizontally averaged height integrated density is important, where the average should be over about 200 km.

The figures show events occurring only after one to two hours of evolution. Beginning the simulations with a perfectly uniform E_s layer, over 200 km, may unrealistically slow the process. Nevertheless, we note that when the

events do finally occur in the simulations they occur suddenly. Hence the apparent time scale of the E_s events will be quite short. Also, because the breaking of the wave is the observable part of the evolution, the apparent horizontal scale of the events may be much less than that of the preceding linear stage evolution.

The phase velocity for Perkins instability modes relative to the F region plasma is zero, and Fejer (1993) reports that the nighttime F region generally drifts to the east. This means that Perkins instability modes should generally propagate to the northeast. As noted by Garcia (2000), and by Kelley and Makela (2001), this is in contradiction to observations of midlatitude MSTIDs made with the Cornell all-sky imager, which show a predominantly southwestward propagation velocity. For this reason the idea that E_s layer induced structuring of the F layer may present with a southwestward trace velocity induced by E_s layer motion is important.

The simulations have produced two main results. The first is that the E_s layer electrodynamic contribution is to produce short lived (15 to 30 min) but large (5 to 20 mV/m) polarization electric fields associated with a breaking wave, and that these produce rapid modulation of the F layer altitude through $\boldsymbol{E} \times \boldsymbol{B}$ drift. Figure 12 shows a simulated event that nearly replicates the Behnke (1979) observation. The F layer altitude rise and the electric field strength appear consistent with the 80 km and 17 mV/m measured by Behnke (1979). In addition, the disturbances were in the form of bands propagating to the southwest. Note that in this case the role of the Perkins instability is only to amplify the seed modulation of the F layer altitude, until it is large enough that the associated polarization electric fields seed the E_s layer instability. The E_s layer instability then imposes an effect on the F layer. Although the ratio Σ_H / Σ_{PF}=3.0 is significantly larger than the average, the Behnke (1979) event boasts the largest electric fields ever measured in the midlatitude F region, so that we require a reason for the conditions that create it to be rare.

The second main result is that in the absence of an E_s layer, the Perkins instability can produce large modulations of the F layer altitude in 2 to 3 h time. This result suggests that concerns regarding the slow growth rate of the Perkins instability, with regard to MSTID phenomena, may be unfounded. The associated electric fields, however, remain small until the F layer altitude modulation exceeds 100 km. That these large altitude modulations occur in the simulations is itself a matter of concern, since there appears to be no observational precedent. Can it be that E_s layers are usually sufficiently dense to inhibit the Perkins instability growth, through the mechanism discussed above? Or, are there some other factors, such as variations in the winds or in the large scale dynamo electric field, which act to interfere with the Perkins instability? Other possibilities include three-dimensional effects, and anomalous effects associated with small-scale structure (Mathews et al., 2001b).

References

Behnke, R.: F layer height bands in the nocturnal ionosphere over Arecibo, J. Geophys. Res., 84, 974–978, 1979.

Bowman, G. G.: Some aspects of sporadic E at mid-latitudes, Planet. Space Sci., 2, 195–211, 1960.

Bilitza, D.: International reference ionosphere, National Space Science Data Center/World Data Center-A for Rockets and Satellites, 1990.

Cathey, E. H.: Some midlatitude sporadic-E results from the Explorer 20 satellite, J. Geophys. Res., 74, 2240–2247, 1969.

Cosgrove, R. B.: Wavelength dependence of the linear growth rate of the E_s layer instability, Ann. Geophys., 25, 1311–1322, 2007, http://www.ann-geophys.net/25/1311/2007/.

Cosgrove, R. B. and Tsunoda, R. T.: Polarization electric fields sustained by closed-current dynamo structures in midlatitude sporadic E, Geophys. Res. Lett., 28, 1455–1458, 2001.

Cosgrove, R. B. and Tsunoda R. T.: Wind-shear-driven, closed-current dynamos in midlatitude sporadic E, Geophys. Res. Lett., 29, 1020, doi:10.1029/2001GL013697, 2002a.

Cosgrove, R. B. and Tsunoda, R. T.: A direction-dependent instability of sporadic-E layers in the nighttime midlatitude ionosphere, Geophys. Res. Lett., 29(18), 1864–1867, 2002b.

Cosgrove, R. B. and Tsunoda, R. T.: Simulation of the nonlinear evolution of the sporadic-E layer instability in the nighttime midlatitude ionosphere, J. Geophys. Res., 108(A7), 1283, doi:10.1029/2002JA009728, 2003.

Cosgrove, R. B. and Tsunoda, R. T.: Instability of the E-F coupled nighttime midlatitude ionosphere, J. Geophys. Res., 109, A04305, doi:10.1029/2003JA010243, 2004a.

Cosgrove, R. B. and Tsunoda, R. T.: Coupling of the Perkins instability and the sporadic E layer instability derived from physical arguments, J. Geophys. Res., 109, A06301, doi:10.1029/2003JA010295, 2004b.

Farley, D. T.: A theory of electrostatic fields in the ionosphere at nonpolar geomagnetic latitudes, J. Geophys. Res., 65, 869–877, 1960.

Fejer, B. G.: F region plasma drifts over Arecibo: solar cycle, seasonal, and magnetic activity effects, J. Geophys. Res. 98(A8), 13 645–13 652, 1993.

Fukao, S., Kelley, M. C., Shirakawa, T., Takami, T., Tamamoto, M., Tsuda, T., and Kato, S.: Turbulent upwelling of the midlatitude ionosphere, 1, Observational results by the MU radar, J. Geophys. Res. 96, 3725–3746, 1991.

Fukao, S., Yamamoto, M., Tsunoda, R. T., Hayakawa, H., and Mukai, T.: The SEEK (Sporadic-E Experiment over Kyushu) Campaign, Geophys. Res. Lett. 25, 1761–1764, 1998.

Garcia, F. J., Kelley, M. C., and Makela, J. J.: Airglow observations of mesoscale low-velocity traveling ionospheric disturbances at midlatitudes, J. Geophys. Res., 105, 18 407–18 415, 2000.

Goodwin, G. L.: The dimensions of some horizontally moving E_s-region irregularities, Planet. Space. Sci., 14, p. 759, 1966.

Goodwin, G. L. and Summers, R. N.: E_s layer characteristics determined from spaced ionosondes, Planet. Space Sci., 18, 1417–1432, 1970.

Haldoupis, C., Schlegel, K., and Farley, D. T.: An explanation for Type 1 radar echoes from the midlatitude *E* region ionosphere, Geophys. Res. Lett., 23, 97–100, 1996.

Haldoupis, C., Kelley, M. C., Hussey, G. C., and Shalimov, S.: Role of unstable sporadic-*E* layers in the generation of midlatitude spread *F*, J. Geophys. Res., 108(A12), 1446, doi:10.1029/2003JA009956, 2003.

Harper, R. M. and Walker, J. C. G.: Comparison of electrical conductivities in the *E* and *F* regions of the nocturnal ionosphere, Planet. Space Sci., 25, 197–199, 1977.

Hines, C. O.: Dynamical heating of the upper atmosphere, J. Geophys. Res., 70, 177–184, 1965.

Hines, C. O.: The upper atmosphere in motion: A selection of papers with annotation, Geophys. Monogr., 18, Am. Geophys. Union, Washington, D.C., 1974.

Hysell, D. L. and Burcham, J. D.: The 30-MHz radar interferometer studies of midlatitude *E* region irregularities, J. Geophys. Res. 105, 12 797–12 812, 2000.

Hysell, D. L., Yamamoto, M., and Fukao, S.: Simulations of plasma clouds in the midlatitude *E* region ionosphere with implications for Type I and Type II quasiperiodic echoes, J. Geophys. Res. 107(A10), 1313, 17-1, doi:10.1029/2002JA009291, 2002.

Hysell, D. L., Larsen, M. F., and Zhou, Q. H.: Common volume coherent and incoherent scatter radar observations of mid-latitude sporadic *E*-layers and QP echoes, Ann. Geophys., 22, 3277–3290, 2004,
http://www.ann-geophys.net/22/3277/2004/.

Johnson, F. S. (Ed.): The Satelite Environment Handbook, Stanford University Press, Stanford, CA, 1961.

Kelley, M. C., Makela, J. J., and Saito, A.: On the electrical structure of airglow depletion/height layer bands over Arecibo, Geophys. Res. Lett. 27(18), 2837–2840, 2000.

Kelley, M. C., and Makela, J. J.: Resolution of the discrepancy between experiment and theory of midlatitude *F*-region structures, Geophys. Res. Lett. 28, 2589–2592, 2001.

Kelley, M. C., Haldoupis, C., Nicolls, M. J., Makela, J. J., Belehaki, A., Shalimov, S., and Wong, V. K.: Case studies of coupling between the *E* and *F* regions during unstable sporadic-*E* conditions, J. Geophys. Res., 108(A12), 1447, doi:10.1029/2003JA009955, 2003.

Klevens, E. H. and Imel, G.: *E* region coupling effects on the Perkins spread *F* instability, J. Geophys. Res., 83, p. 199, 1978.

Kubota, M., Fukunishi, H., and Okana, S.: Characteristics of medium- and large-scale TIDs over Japan derived from OI 630-nm nightglow observation, Earth Planet. Space, 53, 741–751, 2001.

Larsen, M. F., Fukao, S., Yamamoto, M., Tsunoda, R., Igarashi, K., and Ono, T.: The SEEK chemical release experiment: Observed neutral wind profile in a region of sporadic *E*, Geophys. Res. Lett., 25, 1789–1792, 1998.

Larsen, M. F.: Winds and shears in the mesosphere and lower thermosphere: Results from four decades of chemical release wind measurements, J. Geophys. Res., 107(A8), 1215, doi:10.1029/2001JA000218, 2002.

Mathews, J. D., Machuga, D. W., and Zhou, Q.: Evidence for electrodynamic linkages between spread-*F*, ion rain, the intermediate layer, and sporadic *E*: results from observations and simulations, J. Atmos. Solar Terr. Phys., 63, p. 1529, 2001a.

Mathews, J. D., González, S., Sulzer, M. P., Zhou, Q., Urbina, J., Kudeki, E., and Franke, S.: Kilometer-scale layered structures inside spread-*F*, Geophys. Res. Lett., 28, 4167–4170, 2001b.

Miller, K. L. and Smith, L. G.: Incoherent scatter radar observations of irregular structure in midlatitude sporadic-E layers, J. Geophys. Res., 83, 3761–3775, 1978.

Perkins, F.: Spread *F* and ionospheric currents, J. Geophys. Res., 78, 218–226, 1973.

Rees, D.: COSPAR international reference atmosphere: 1986 part I: Thermosphere models, Adv. Space Res., 8(5–6), Pergamon Press, 1988.

Rosado-Roman, J. M., Swartz, W. E., and Farley, D. T.: Plasma instabilities observed in the *E* region over Arecibo and a proposed nonlocal theory, J. Atmos. Solar Terr. Phys., 66, 1593–1602, 2004.

Rosenberg, N. W.: Dynamic model of ionospheric wind profiles, J. Geophys. Res., 73, 4965–4968, 1968.

Saito, A., Nishimura, M., Yamamoto, M., Fukao, S., Kubota, M., Shiokawa, K., Otsuka, Y., Tsugawa, T., Ogawa, T., Ishii, M., Sakanoi, T., and Miyazaki, S.: Traveling ionospheric disturbances detected in the FRONT campaign, Geophys. Res. Lett., 28(4), 689–692, 2001.

Seyler, C. E., Rosado-Roman, J. M., and Farley, D. T.: A nonlocal theory of the gradient-drift instability in the ionospheric *E*-region plasma at midlatitudes, J. Atmos. Solar Terr. Phys., 66, 1627–1637, 2004.

Shalimov, S., Haldoupis, C., and Schlegel, K.: Large polarization electric fields associated with midlatitude sporadic *E*, J. Geophys. Res. 103, 11 617–11 625, 1998.

Shalimov, S. and Haldoupis, C.: *E*-region wind-driven electrical coupling of patchy sporadic-*E* and spread-*F* at midlatitude, Ann. Geophys., 23, 2095–2105, 2005,
http://www.ann-geophys.net/23/2095/2005/.

Shiokawa, K., Ihara, C., Otsuka, Y., and Ogawa, T.: Statistical study of nighttime medium-scale travelling ionospheric disturbance using midlatitude airglow images, J. Geophys. Res. 108(A1), p. 1052, 2003.

Smith, L. B.: Rotation of wind direction with altitude as obtained from vapor-trail observations, J. Geophys. Res., 77, 2927–2933, 1972.

Spreiter, J. R. and Briggs, B. R.: Theory of electrostatic fields in the ionosphere at polar and middle geomagnetic latitudes, J. Geophys. Res., 66, 1731–1744, 1961.

Stephani, H.: Differential Equations: Their Solution Using Symmetries, Cambridge University Press, 1995.

Swartz, W. E., Collins, S. C., Kelley, M. C., Makela, J. J., Kudeki, E., Franke, S., Urbina, J., Aponte, N., Gonzalez, S., Sulzer, M. P., and Friedman, J. S.: First observations of an *F*-region turbulent upwelling coincident with severe *E*-region plasma and neutral atmosphere perturbations, J. Atmos. Solar Terr. Phys., 64, 1545–1556, 2002.

Tsunoda, R.: On polarized frontal structures, type-1 and quasi-periodic echoes in midlatitude sporadic *E*, Geophys. Res. Lett., 25, 2614–2617, 1998.

Tsunoda, R. T. and Cosgrove, R. B.: Coupled electrodynamics in the nighttime midlatitude ionsphere, Geophys. Res. Lett., 28,

4171–4174, 2001.

Tsunoda, R. T., Cosgrove, R. B., and Ogawa, T.: Azimuth-dependent E_s layer instability: A missing link found, J. Geophys. Res., 109, A12303, doi:10.1029/2004JA010597, 2004.

Wakabayashi, M., Ono, T., Mori, H., and Bernhardt, P. A.: Electron density and plasma waves in mid-latitude sporadic-E layer observed during the SEEK-2 campaign, Ann. Geophys., 23, 2335–2345, 2005,
http://www.ann-geophys.net/23/2335/2005/.

Whitehead, J. D.: Recent work on mid-latitude and equatorial sporadic-E, J. Atmos. Solar Terr. Phys. 8(5), 401–424, 1989.

Yamamoto, M., Komoda, N., Fukao, S., Tsunoda, R., Ogawa, T., and Tsuda, T.: Spatial structure of the E region field-aligned irregularities revealed by the MU radar, Radio Sci., 29(1), p 337, 1994.

Yamamoto, M., Kumura, F., Fukao, S., Tsunoda, R. T., Igarashi, K., and Ogawa, T.: Preliminary results from joint measurements of E-region field-aligned irregularities using the MU radar and the frequency-agile radar, J. Atmos. Solar Terr. Phys., 59, 1655–1663, 1997.

Yamamoto, M., Ono, T., Oya, H., Tsunoda, R. T., Larsen, M. F., Fukao, S., and Yamamoto, M.: Structures in sporadic-E observed with an impedance probe during the SEEK campaign: Comparisons with neutral-wind and radar-echo observations, Geophys. Res. Lett. 25, 1781–1784, 1998.

Yokoyama, T., Yamamoto, M., Fukao, S., and Cosgrove, R. B.: Three-dimensional simulation on generation of polarization electric field in the midlatitude E-region ionosphere, J. Geophys. Res. 109, A01309, doi:10.1029/2003JA010238, 2004.